ACBP/DBI protein neutralization confers autophagy-dependent organ protection through inhibition of cell loss, inflammation, and fibrosis

Omar Motiño, Flavia Lambertucci, Gerasimos Anagnostopoulos, Sijing Li, Jihoon Nah, Francesca Castoldi, Laura Senovilla, Léa Montégut, Hui Chen, Sylvère Durand, et al.

PNAS

Main Manuscript for

ACBP/DBI protein neutralization confers autophagy-dependent organ protection through inhibition of cell loss, inflammation and fibrosis

Omar Motiño[1-2], Flavia Lambertucci[1-2*], Gerasimos Anagnostopoulos[1-3*], Sijing Li[1-3*], Jihoon Nah[4], Francesca Castoldi[5], Laura Senovilla[1-2,6], Léa Montégut[1-3], Hui Chen[1-2], Sylvère Durand[1-2], Mélanie Bourgin[1-2], Fanny Aprahamian[1-2], Nitharsshini Nirmalathasan[1-2], Karla Alvarez-Valadez[1-3], Allan Sauvat[1-2], Vincent Carbonnier[1], Mojgan Djavaheri-Mergny[1-2], Federico Pietrocola[5], Junichi Sadoshima[4], Maria Chiara Maiuri[1-2], Isabelle Martins[1-2#], and Guido Kroemer[1-2, 7-8#]

[1] Centre de Recherche des Cordeliers, Equipe labellisée par la Ligue contre le cancer, Université de Paris, Sorbonne Université, Inserm U1138, Institut Universitaire de France, Paris, France.

[2] Metabolomics and Cell Biology Platforms, Institut Gustave Roussy, Villejuif, France.

[3] Faculté de Médecine, Université de Paris Saclay, Kremlin Bicêtre, France.

[4] Department of Cell Biology & Molecular Medicine, New Jersey Medical School- Rutgers, The State University of New Jersey, Newark, NJ, USA.

[5] Department of Bioscience and Nutrition, Karolinska Institute, Huddinge, Sweden.

[6] Unidad de Excelencia Instituto de Biología y Genética Molecular (IBGM), Universidad de Valladolid - CSIC, Valladolid, Spain.

[7] Pôle de Biologie, Hôpital Européen Georges Pompidou, AP-HP, Paris, France.

[8] Lead contact.

[#]Correspondence: Guido Kroemer (Kroemer@orange.fr) or Isabelle Martins (isabelle.martins@inserm.fr).

[*]These authors contributed equally to this work.

Author Contributions: G.K. and O.M. designed the study. G.K. and O.M wrote the paper. O.M., F.L., G.A., S.L., J.N. F.C., L.S., L.M., and H.C. performed mouse studies. S.L. and V.C. performed the bioinformatic analyses. S.D., F.A., M.B. and N.N. performed the metabolomic analyses. K.A-V.

and A.S. performed the image analysis. I.M., M.C.M., J.S., F.P., and M.D-M. provided intellectual input and edited the paper. All authors reviewed the results, edited, and approved the final version of the manuscript.

Competing Interest Statement: GK has been holding research contracts with Daiichi Sankyo, Eleor, Kaleido, Lytix Pharma, PharmaMar, Samsara, Sanofi, Sotio, Tollys, Vascage and Vasculox/Tioma. GK is on the Board of Directors of the Bristol Myers Squibb Foundation France. GK is a scientific co-founder of everImmune, Samsara Therapeutics and Therafast Bio. GK is the inventor of patents covering therapeutic targeting of aging, cancer, cystic fibrosis and metabolic disorders. GK and OM are inventors of a patent covering the therapeutic use of anti-ACBP/DBI antibodies. GK is the founder of OsasunaTherapeutics, which targets ACBP/DBI.

Classification: Biological sciences, Cell Biology, Biochemistry, Metabolism, Immunology and Inflammation.

Keywords: Acyl-CoA Binding Protein, autophagy, non-alcoholic steatohepatitis, myocardium infarction, liver fibrosis, lung fibrosis.

Abstract

Acyl-CoA binding protein (ACBP), also known as diazepam-binding inhibitor (DBI), is an extracellular feedback regulator of autophagy. Here, we report that injection of a monoclonal antibody neutralizing ACBP/DBI (α-DBI) protects the murine liver against ischemia/reperfusion damage, intoxication by acetaminophen and concanavalin A, non-alcoholic steatohepatitis caused by methionine/choline deficient diet, as well as against liver fibrosis induced by bile duct ligation or carbon tetrachloride. α-DBI downregulated pro-inflammatory and profibrotic genes and upregulated antioxidant defenses and fatty acid oxidation in the liver. The hepatoprotective effects of α-DBI were mimicked by the induction of ACBP/DBI-specific autoantibodies, an inducible *Acbp/Dbi* knockout or a constitutive *Gabrg2*^{F77I} mutation that abolishes ACBP/DBI binding to the $GABA_A$ receptor. Liver protective α-DBI effects were lost when autophagy was pharmacologically blocked or genetically inhibited by knockout of *Atg4b*. Of note, α-DBI also reduced myocardium infarction and lung fibrosis, supporting the contention that it mediates broad organ-protective effects against multiple insults.

Significance Statement

Pharmacological induction of autophagy usually involves small molecules targeting intracellular signaling cascades. Here, Motiño et al. demonstrate that monoclonal antibody-mediated neutralization of an extracellular inhibitor of autophagy, ACBP/DBI, stimulates cytoprotective autophagy, hence inhibiting cell loss, inflammation and fibrosis in various disease models affecting liver, lung and myocardium. Extracellular ACBP/DBI acts as an autophagy checkpoint on $GABA_A$ receptors, hence offering a target for a new class of "autophagy checkpoint inhibitors.

Main Text

Introduction

Macroautophagy (hereafter referred to as 'autophagy') is a process through which portions of the cytoplasm are sequestered in autophagosomes, which subsequently fuse with lysosomes for the enzymatic hydrolysis of the autophagic cargo (1). Although autophagy is often observed in the context of cell death, it preponderantly subserves cytoprotective functions. Thus, excessive autophagy leading to cellular demise ('autophagic cell death' or 'autosis') is a rare phenomenon. Rather, in most instances, cell stress-induced autophagy delays or avoids cell death by facilitating cellular adaptation (2–4). This stress-adaptive function of autophagy results from a combination of factors, including but not limited to (i) the mobilization of macromolecules including proteins, mRNA, lipids and glycogen to generate energy-rich metabolites and building blocks for anabolic reactions, and (ii) the selective removal of damaged cellular structures including aggregates of misfolded proteins, uncoupled or permeabilized mitochondria, as well as other dysfunctional organelles (4–6). As a result, cellular fitness is improved in a cell-autonomous fashion. Moreover, the activation of pro-inflammatory pathways is blunted by autophagy due to the removal of molecules (such as cytosolic DNA or reactive oxygen species) that may activate endogenous pattern recognition receptors, as well as due to the downregulation of the downstream signals emanating from such receptors (2, 7, 8).

Given its preponderant role in the turnover of cytoplasmic structures, experimental inhibition of autophagy accelerates the time-dependent degeneration of organelles, cells, organs and the entire organism. Genetic defects that attenuate autophagy can specifically affect distinct organs or cause multi-organ syndromes (9, 10). Moreover, normal aging and obesity, the most prevalent pathological condition in humans, are associated with reduced autophagic flux (11). Conversely, genetic manipulations aiming at inducing autophagy have a broad antiaging effect, as this has been demonstrated in mice by transgenic overexpression of the essential autophagy gene *Atg5* (12) or by gain-of-function mutation of *Beclin 1* (13). Of note, it appears that many lifespan- and healthspan-extending manipulations, be they nutritional (such as caloric restriction or oral supplementation with spermidine), pharmacological (such as administration of rapamycin) or genetic (such as interruption of the insulin/insulin growth factor receptor or removal of tumor suppressor protein p53, TP53) require autophagy for being efficient (14–19). In view of these rather broad health-improving effects of autophagy, its induction has been proposed as a general strategy to combat diseases affecting specific organs including liver (11, 20, 21)**,** heart (22), lung (23) or kidney (24, 25). As an example, autophagy induction can prevent the development of multiple hepatic pathologies including but not limited to acetaminophen-induced liver failure (26), non-

alcoholic hepatosteatosis (NASH) (27), liver fibrosis and cirrhosis induced by alcohol or toxins (28), as well as cholestasis-induced hepatitis (21).

The pharmacological induction of autophagy is typically achieved by drugs acting on intracellular energy sensors including mechanistic target of rapamycin complex 1 (MTORC1) and E1A-associated protein (EP300), which must be inhibited to induce autophagy, and sirtuin-1 (SIRT1) or AMP-activated kinase (AMPK), which must be activated to induce autophagy (19, 29, 30). Other classes of autophagy inducers disrupt the inhibitory interaction of B-cell lymphoma 2 (BCL2) with the pro-autophagic lipid kinase complex composed by Beclin-1 and phosphatidylinositol 3-kinase catalytic subunit type 3 (PIK3C3) (31) or activate the lysosomal calcium channel TRPML1 (32).

Recently, we described an extracellular feedback loop of autophagy that involves the protein acyl coenzyme A binding protein (ACBP), which is called by diazepam-binding inhibitor (DBI) (10). Indeed, autophagy is tied to the atypical secretion of this leaderless protein that is predominantly present in the cytosol of nucleated cells (10, 33). Once released into the extracellular space, ACBP/DBI then acts on gamma-aminobutyric acid (GABA) receptors to inhibit autophagy via autocrine, paracrine and neuroendocrine pathways (10, 34). When injected intraperitoneally or intravenously, a monoclonal antibody (mAb) against ACBP/DBI (dubbed as α-DBI) remarkably reduced high-fat diet induced adiposity, diabetes and hepatosteatosis, while enhancing autophagy, lipolysis and β-oxidation and simultaneously reducing appetite (10, 34, 35). These effects were considered to be on target because they could be mimicked by inducible whole-body knockout of ACBP/DBI (10). Intrigued by these observations, we decided to investigate the potential of α-DBI on different organs (liver, heart, lung) damaged by a series of drugs, toxins or ischemic insults. Here, we report the broad organ-protective, autophagy-dependent effects of α-DBI.

Material and Methods

We used mouse models of cardiac ischemia (induced by ligation of the left anterior descending coronary artery (LAD) (36), liver ischemia reperfusion (37), NASH induced by a methionine choline-deficient diet (MCD, as opposed to regular chow diet, RCD), liver fibrosis (induced by bile duct ligation or CCL4 injections) (38, 39) and lung fibrosis (induced by bleomycin) (40). Data are expressed as means ± SEM. For experimental and statistical details see Supplemental Information.

Results

Hepato- and cardio-protective effects of ACBP/DBI neutralization against acute insults. Injection of a monoclonal antibody (mAb) neutralizing ACBP/DBI (α-DBI) (2.5 µg/g intraperitoneally, i.p., 6 and 2 hours before sacrifice) enhances the hepatic lipidation of microtubule-associated proteins 1A/1B light chain 3B (hereafter referred to as LC3B), a marker of autophagy, giving rise to the electrophoretically more mobile LC3-II form (Fig. 1A,B) (41). This effect was further enhanced by injection of the lysosomal protease inhibitor leupeptin (30 mg/kg i.p. 2 hours before sacrifice), corroborating the elevated autophagic flux (42) (Fig. 1A,B). Accordingly, a single injection of α-DBI (2.5 µg/g i.p. 4 hours before sacrifice) induced the formation of autophagic puncta in hepatocytes from mice expressing a transgene encoding a green fluorescent protein (GFP)-LC3 fusion protein (41) (Fig. 1C,D). Two injections of α-DBI (Fig. 1E) also reduced the histological signs of ischemia/reperfusion (congestion, ballooning, necrosis summed up in the Suzuki score) (43) of the liver (Fig. 1F,G), as well as an increase in the plasma concentrations of the two transaminases alanine aminotransferase (ALT) and aspartate aminotransferase (AST) (Fig. 1H,I). When α-DBI injection was combined with hydroxychloroquine (50 mg/kg), a lysomotropic agent that inhibits autophagy *in vivo* (44), the hepatoprotective effects of ACBP/DBI neutralization against ischemia/reperfusion were lost (Fig. 1F-I). Similar hydroxychloroquine-inhibitable, hepatoprotective effects of α-DBI were obtained in two models of pharmacological hepatotoxicity caused by acetaminophen (APAP, trade name: paracetamol) and the lectin concanavalin A (ConA) (Fig. S1A). In both models, α-DBI reduced histological signs of hepatic injury (Fig. S1B,C,F,G), as well as circulating transaminase levels (Fig. S1D,E,H,I). Importantly, α-DBI also induced signs of autophagic flux in the myocardium (Fig. 2A,B) including signs of mitophagy, as measured by means of the fluorescent biosensor Mito-Keima (45) (Fig. 2C,D). Moreover, α-DBI injection (Fig. 2E) reduced myocardial infarction provoked by ligation of the left coronary artery, and this cardioprotective effect was lost when the essential autophagy gene *Atg7* was floxed and selectively knocked out in heart by a CRE recombinase specifically expressed in cardiomyocytes (genotype: *αMHC-Cre*::*Atg7*$^{f/f}$) (Fig. 2F,G).

In conclusion, mAb-mediated neutralization of ACBP/DBI induces autophagy in the liver and in the heart and protects hepatocytes and cardiomyocytes against acute damage in an autophagy-dependent fashion.

NASH-preventive effects of immunological or genetic ACBP/DBI inhibition. ACBP/DBI neutralization attenuates high-fat diet (HFD)-induced nonalcoholic fatty liver disease (NAFLD) (10). However, since ACBP/DBI neutralization also reduces HFD-induced obesity (10), it is not clear whether this liver protective effect is direct or secondary to weight reduction. Here, we investigated

the effects of ACBP/DBI neutralization on a model of NASH that occurs in the context of weight loss, as the result of a methionine/choline-deficient diet (MCD; control: regular chow diet, RCD) (38). NASH features were evaluated after a 4-week course of MCD in mice receiving weekly injections of α-DBI (control: isotype IgG mAb) or in the context of a tamoxifen-inducible whole-body knockout of floxed *Acbp/Dbi*$^{-/-}$ (genotype: *UBC-cre/ERT2*::*Acbp/Dbi*$^{f/f}$, control: *Acbp/Dbi*$^{f/f}$ without CRE) (Fig. 3A). MCD results in the accumulation of the autophagic substrate sequestosome 1 (SQSTM1, best known as p62), suggesting reduced autophagic flux, and this effect was reversed by α-DBI (Fig. 3B,C). Accordingly, α-DBI increased LC3B lipidation as a sign of autophagy induction (Fig. 3B,D). α-DBI largely prevented the histological (steatosis, ballooning, and inflammation) and enzymological signs (ALT and AST) of NASH induced by MCD (Fig. 3E-H). Genetic ablation of *Acbp/Dbi* similarly protected against MCD-associated NASH as it increased autophagic flux (Fig. 4I-K) and obviated the MCD-induced histopathological alterations (Fig. 3L,M) as well as the transaminase elevation (Fig. 3N,O). Of note, in these experiments, both α-DBI and the *Acbp/Dbi* knockout reduced the spontaneous weight gain of mice kept on RCD, but counteracted the weight loss caused by MCD (Fig.S2A,C). Moreover, α-DBI caused a reduction in the liver *Acbp/Dbi* mRNA levels, though less than the *Acbp/Dbi* knockout (Fig. S2B,D). Alternately, we neutralized ACBP/DBI by a third protocol consisting in the autoimmunization of mice with recombinant ACBP/DBI fused to the potent immunoadjuvant keyhole limpet hemocyanin (KLH) (Fig. S2E) (10, 46). Prophylactic induction of ACBP/DBI-specific autoantibodies also ameliorated the induced weight loss and *Acbp/Dbi* mRNA expression (Fig. S2F,G), and reversed the MCD-induced autophagic blockade (Fig. S2H-J), as well as the signs of NASH (Fig.S2K-M). Finally, we took advantage of mice in which the γ2 subunit of $GABA_A$ receptor is mutated (F77I) to abolish ACBP/DBI binding (47). Such mice were relatively resistant against MCD-induced NASH (Fig. S2N-P).

Altogether these results indicate that four different methods of ACBP/DBI inhibition (passive neutralization with α-DBI, active autoimmunization, genetic knockout, mutation of the ACBP/DBI receptor) similarly protect against NASH.

Transcriptional correlates of the NASH-preventive effects of ACBP/DBI inhibition. Bulk RNAsequencing (RNAseq) of the livers from mice receiving RCD or MCD together with IgG control or α-DBI revealed that most of the MCD-induced alterations in mRNA expression were reversed by α-DBI (Fig. S3A). Volcano plots followed by gene ontology (GO) analyses revealed that, in the context of MCD, α-DBI downregulated multiple gene set associated with inflammation and carcinogenesis, but upregulated genes involved in fatty acid and drug metabolism as well as in peroxisomes and autophagy (Fig. S3B,C, Fig. S4A). The effects of α-DBI on the liver transcriptome of RCD-fed mice were relatively scarce compared to its effects on MCD-fed rodents (Fig. S3A, Fig. S4B,C). To validate these findings, we performed immunohistochemical detection of the

macrophage marker F4/80. α-DBI prevented the increase in hepatic macrophage infiltration that is usually observed after MCD (Fig. S3D,E). Moreover, RT-qPCR analyses confirmed that α-DBI had relatively small effects on normal (RCD) livers, that MCD (compared to RCD) associates with an upregulation of multiple pro-inflammatory genes (*Cd68*, *F480*, *Il1b*, *Il6*, *Mcp1*, *Nlrp3*, *Tnfa*), but a downregulation of antioxidant genes (*Cat*, *Gpx*, *Gsr*, *Hmox1*, *Nfr2 Sod1*, *Sod2*) and that most (if not all) of these effects are reversed by α-DBI (Fig. S3F). The anti-inflammatory effects of α-DBI were validated by measuring plasma concentrations of CCL4, CCL2 (MCP-1), CCXL10 and TNFA (Fig. S5A). Moreover, the protein levels of CAT and HMOX1 were elevated in α-DBI-treated mice under MCD as compared to isotype control mice receiving the same diet, commensurate with an increased abundance of nuclear (but reduced abundance of cytosolic) NRF2 (Fig. S5B-D), which is the master transcription factor of antioxidant defense (48).

The RT-qPCR-detectable reversal of MCD-associated effects in liver mRNA expression was further corroborated when ACBP/DBI was inhibited by autoantibodies following the autoimmunization with ACBP/DBI-KLH conjugates (Fig. S4D) or by tamoxifen-inducible knockout of *Acbp/Dbi* (Fig. S4E). Mass spectrometric metabolomics revealed that MCD was coupled to an decrease in several lipid species in the liver and that this decrease was counteracted by α-DBI, as particularly evident for carnitine-conjugate fatty acids (Fig. 4A, Fig. S6A,B). Accordingly, MCD was coupled to a downregulation of carnitine palmitoyl transferase 1 (CPT1), the mitochondrial outer membrane transporter that is rate limiting for β-oxidation and the inhibition of which causes the depletion of acylcarnitines (49, 50). This MCD-induced downregulation of CPT1 was observed at the protein and mRNA levels and was reversed by α-DBI (Fig. 4B,C). MCD also caused the α-DBI -repressible downregulation of *Ppara* (a transcription factor essential for β-oxidation) (51, 52) at the mRNA (Fig. 4D) and protein levels (Fig. S5E).

In sum, ACBP/DBI inhibition close-to-fully reverses the transcriptional alterations associated with MCD-induced NASH. Of note, the genes that were significantly downregulated by ACBP/DBI neutralization in the context of MCD-triggered murine NASH significantly overlapped with genes that are upregulated in human NAFLD or NASH compared to normal livers across 10 different datasets (Table S1), pointing to the translational relevance of these results.

Mechanisms of the anti-NASH effects of ACBP/DBI neutralization. To understand the contribution of autophagy to the anti-NASH effects of α-DBI, we took advantage of mice bearing a partial autophagy defect due to the constitutive knockout of *Atg4b* (genotype: *Atg4b*$^{-/-}$) (53) (Fig. S6C). These mice were not more susceptible to NASH induction by MCD than wild type (*Wt*) mice (Fig. 4E-K). However, *Atg4b*$^{-/-}$ mice were relatively resistant to autophagy induction by α-DBI, as well as to the anti-NASH, and body weight-restoring effects of α-DBI (Fig. 4E-K, Fig. S6D). RT-qPCR analyses confirmed that, in MCD-fed WT mice, α-DBI induced antioxidant genes and

downregulated pro-inflammatory factors as well as *Acbp/Dbi* mRNA (Fig. 4L, Fig. S6E). These effects were much attenuated in *Atg4b*$^{-/-}$ mice (Fig. 4L), supporting the contention that autophagy is required for the transcriptional effects of ACBP/DBI neutralization.

Next, we evaluated the capacity of α-DBI to reverse (rather than to prevent) NASH by treating mice with established NASH (4 weeks of MCD) by means of 2 injections of the mAb together with a dietary normalization to RCD (Fig. S7). In this model, the MCD→RCD switch caused partial reversion (R) of NASH, and this effect was significantly enhanced by α-DBI at the histological (Fig. 5A,B), enzymological (Fig. 5C,D), transcriptomic levels (Fig. 5E-G), as well as the level of body weight recovery (Fig. S7C). Moreover, α-DBI improved the recovery of carnitine species (Fig. 5H,I), commensurate with an upregulation of CPT1A and the stimulation of autophagic flux (Fig. S7F,G). In the next step, we determined whether inhibition of CPT1A (pharmacologically with etomoxir) and autophagy (genetically by *Atg4b*$^{-/-}$) interferes with the beneficial effects of α-DBI on recovery from NASH (Fig. S7A,B). At the histological level, etomoxir or *Atg4b* knockout all attenuated the curative effects of α-DBI (Fig. 5J-N). Of note, etomoxir failed to interfere with induction of autophagic flux by α-DBI (Fig. S7H-I, K-L). Conversely, etomoxir treated and *Atg4b*$^{-/-}$ mice exhibited an attenuated upregulation of *Cpt1a* mRNA (among other genes relevant to β-oxidation) and protein levels (Fig. S7H-M).

Altogether, these results suggest that both CPT1A and autophagy are required for the anti-NASH effects of α-DBI. Apparently, autophagy operates upstream of CPT1A because autophagy inhibition curtails α-DBI-induced CPT1A upregulation, while direct CPT1A inhibition fails to suppress α-DBI-induced autophagy.

ACBP/DBI neutralization suppresses fibrosis of liver and lung. HFD and MCD largely fail to induce liver fibrosis and cirrhosis, which is observed when human NASH progresses (54). For this reason, we turned to a model in which liver fibrosis is induced by bile duct ligation (BLD) (55). Two weeks post-BLD, hepatic damage and fibrosis was prominent in isotype control antibody-treated mice, but much attenuated after biweekly injection of α-DBI (Fig. 6A-D). Similar results were obtained with the well-established model of carbon tetrachloride (CCl_4)-induced liver fibrosis, which was modulated by weekly administration of α-DBI (or isotype IgG control for 9 weeks) and/or daily injections of hydroxychloroquine (or vehicle control during the last 4 weeks of the experiment) (Fig. 6E). In this model, α-DBI attenuated weight loss (Fig. S8A), signs of fibrosis detectable by Sirius red staining (Fig. 6F,G) or quantification of the collagen-enriched amino acid hydroxyproline (Fig. S8B), as well as hepatic damage reflected by transaminase ALT activity (Fig. 6H and S8C), and by immunoblot detection of the pro-fibrotic markers collagen 1A1 and α-smooth muscle actin (α-SMA) (Fig. S8D-F). The beneficial effects of α-DBI on liver damage and fibrosis were lost when autophagy was inhibited by hydroxychloroquine (Fig. 6F-G, Fig. S8D-F). The CCl_4-induced alterations in p62

and LC3-II were reversed by α-DBI, but only in the absence of hydroxychloroquine, not in its presence (Fig. S8G-I). α-DBI also reversed the CCl_4-induced elevation of circulating transaminases, again only in the absence of hydroxychloroquine (Fig. 6H and S8C). Moreover, α-DBI reversed most if not all of the transcriptional effects of chronic CCl_4 intoxication, thus reducing the expression of pro-fibrotic, pro-inflammatory, macrophage associated or transforming growth factor-β (TGF-β)-relevant genes, but enhancing that of anti-oxidant enzymes. These transcriptional effects of α-DBI were abolished when hydroxychloroquine was co-administered (Fig. 6I). In a further set of experiments, we determined whether CCl_4-induced liver fibrosis can be reversed more efficiently when CCl_4 withdrawal is combined with weekly injections of α-DBI for 4 weeks (Fig. 7A). Again, in this curative setting, α-DBI reduced damage signs of hepatic fibrosis (Fig. 7B-E).

Altogether, these data indicate that ACBP/DBI neutralization has beneficial effects on liver fibrosis that largely depend on autophagy. Of note, in a model of bleomycin-induced lung fibrosis, α-DBI alleviated the histological signs of tissue damage, while reducing upregulation of collagen-encoding genes and macrophage-associated genes (Fig. 8A-E), supporting the contention that, beyond its hepatoprotective action, α-DBI has systemic antifibrotic effects.

Discussion

ACBP/DBI is secreted by eukaryotic cells upon induction of autophagy and then restrains autophagy by local (autocrine/paracrine) and neuroendocrine circuitries (10, 56, 57). As a result, systemic injection of a neutralizing ACBP/DBI-specific mAb (α-DBI) induces autophagy in mouse tissues including heart, liver, and lung. These effects are observed within hours and hence cannot be attributed to a reduction of food intake secondary to the blockade of orexigenic ACBP/DBI effects. We have found in the past that α-DBI reduces appetite in specific circumstances (such as after a 24-hour starvation period or in high-fat diet-induced obesity). However, α-DBI administration actually reduced the weight loss associated with MCD or chronic CCl_4 intoxication, yet induced autophagy in these conditions. Hence, the autophagy-stimulatory effects of α-DBI do not rely on its appetite-suppressive effects.

As mentioned in the Introduction, autophagy induction has broad health-improving effects resulting from its capacity to improve cellular fitness and metabolism (2, 4–6, 8). As shown in this paper, α-DBI ameliorates ischemic tissue damage in the heart and the liver, attenuates acute hepatotoxicity of acetaminophen and concanavalin A, prevents and reverses MCD-induced NASH, and also displays antifibrotic activity in models of BDL or CCl_4-induced liver fibrosis and bleomycin-induced lung fibrosis. These beneficial effects are suppressed by high-dose hydroxychloroquine or by knockout of *Atg4b* (or that of *Atg7* in the heart), supporting the contention that they truly depend on the induction of autophagy (Fig.9). Mass spectrometric metabolomics indicated that the anti-NASH activity of α-DBI was accompanied by an increase in hepatic acylcarnitines, suggestive of enhanced CPT1A activity and fatty acid oxidation. Indeed, inhibition of CPT1A abolished the beneficial effect of α-DBI on NASH, yet failed to interfere with autophagy induction by α-DBI. Conversely, inhibition of autophagy blocked the MCD-induced upregulation of CPT1A, suggesting that this enzyme operates downstream of autophagy to antagonize NASH.

Remarkably, α-DBI reversed most of the alterations in gene transcription associated with MCD-induced NASH in mice. A significant fraction of the α-DBI-repressed genes are associated with human NASH or NAFLD, supporting the possible clinical relevance of these results. In general, it appears that α-DBI antagonizes the NASH or liver fibrosis-associated upregulation of pro-inflammatory and pro-fibrotic genes, as it prevents the downregulation of genes involved in fatty acid and drug metabolism as well as in peroxisomes and autophagy. Such gene-regulatory effects of α-DBI are largely blocked by hydroxychloroquine or *Atg4b* knockout, supporting the idea that they result from autophagy induction. Since α-DBI dramatically improved the histological signs of tissue damage including local inflammation, it appears plausible that the transcriptional shifts

induced by α-DBI reflect maintenance of general tissue homeostasis rather than cell-autonomous epigenetic effects of autophagy. That said, α-DBI also influenced the expression of some genes in mice under RCD, hence upregulating *Ppara* and downregulating *Dbi*. This latter phenomenon might be explained by the interruption of a feedforward loop in which ACBP/DBI induces the expression of further ACBP/DBI in the liver (58).

Close-to-total and irreversible removal of ACBP/DBI by genetic means has no detectable effects on adult mice housed under standard conditions (10). Thus, in contrast to the constitutive knockout of ACBP/DBI (59), knockout of ACBP does not compromise the skin barrier function in adult mice (35), suggesting that mAB-mediated blockade of ACBP/DBI should be well tolerated without major side effects. Accordingly, we did not detect any macroscopic or histological signs of toxicity associated with repeated α-DBI administrations. Moreover, induction of polyclonal autoantibodies capable of neutralizing ACBP/DBI failed to induce visible side effects over several months. It is remarkable, however, that the liver disease-attenuating effects of α-DBI are mimicked by those of the inducible *Dbi* knockout, constitutive mutation of the ACBP/DBI receptor, as well as by the induction of autoantibodies, strongly arguing in favor of the hypothesis that α-DBI acts on-target rather than by recognizing additional host genome-encoded or microbial proteins that structurally resemble ACBP/DBI (60, 61).

ACBP/DBI plasma concentrations increased with age in humans (34), and knockout of its orthologues increases lifespan in yeast and nematodes (62, 63) and delays leaf senescence in plants while inducing autophagy (64). Aging is coupled to a progressive decline in autophagic flux, and genetic or pharmacological induction of autophagy extends lifespan and healthspan in model organisms including mice (13, 15). Hence, at a speculative level, it might be attempted to neutralize ACBP/DBI to minimize the age-associated reduction in autophagy and to postpone the manifestation of age-associated diseases. This possibility should be explored in future studies.

As a general rule in pharmacology, antagonists of inhibitory pathways have fewer side effects than agonists of activating pathways. Thus, so-called immune checkpoint inhibitors (ICIs) have been developed for numerous oncological indications to induce anticancer immune responses by targeting immunosuppressive surface molecules including CTLA-4, PD-1 and PD-L1. In sharp contrast, direct immunostimulators acting on pattern recognition receptors have largely failed in the field of immuno-oncology (65, 66). By analogy to ICIs, α-DBI, an antibody that blocks an inhibitory circuitry normally restraining autophagy, might be considered as an autophagy checkpoint inhibitor (ACI). It remains to be seen, however, whether such ACIs targeting ACBP/DBI will be developed for clinical applications.

Data Availability

All study data are included in the article and SI Appendix. Additional data is available at the Gene Expression Omnibus at accession number GSE194346.

Acknowledgments

We thank Dr. Paule Opolon (Department of Pathology, Gustave Roussy, Villejuif, France) for histopathological analysis. We thank the core facilities of Centre de Recherche des Cordeliers and Gustave Roussy for technical support. GK is supported by the Ligue contre le Cancer (équipe labellisée); Agence National de la Recherche (ANR) – Projets blancs; AMMICa US23/CNRS UMS3655; Association pour la recherche sur le cancer (ARC); Association “Ruban Rose”; Cancéropôle Ile-de-France; Fondation pour la Recherche Médicale (FRM); a donation by Elior; Equipex Onco-Pheno-Screen; European Joint Programme on Rare Diseases (EJPRD); Gustave Roussy Odyssea, the European Union Horizon 2020 Projects Oncobiome and Crimson (No. 101016923); Fondation Carrefour; Institut National du Cancer (INCa); Inserm (HTE); Institut Universitaire de France; LabEx Immuno-Oncology (ANR-18-IDEX-0001); the Leducq Foundation; a Cancer Research ASPIRE Award from the Mark Foundation;, the RHU Torino Lumière; Seerave Foundation; SIRIC Stratified Oncology Cell DNA Repair and Tumor Immune Elimination (SOCRATE); and SIRIC Cancer Research and Personalized Medicine (CARPEM). This study contributes to the IdEx Université de Paris ANR-18-IDEX-0001. GA is supported by the Fondation pour la Recherche Médicale (FRM). LS is supported by Beatriz Galindo senior program of the Spanish Ministry of Universities; Strategic Program “Instituto de Biología y Genética Molecular (IBGM), Junta de Castilla y León” (Ref. CCVC8485) and Internationalisation Project of the "Unidad de Excelencia Instituto de Biología y Genética Molecular (IBGM) of Valladolid" (Ref. CL-EI-2021).

References

1. H. Morishita, N. Mizushima, Diverse Cellular Roles of Autophagy. *Annu Rev Cell Dev Biol* **35**, 453–475 (2019).

2. L. M. Schwartz, Autophagic Cell Death During Development - Ancient and Mysterious. *Front Cell Dev Biol* **9** (2021).

3. G. Kroemer, B. Levine, Autophagic cell death: the story of a misnomer. *Nat Rev Mol Cell Biol* **9**, 1004–1010 (2008).

4. C. López-Otín, G. Kroemer, Hallmarks of Health. *Cell* **184**, 33–63 (2021).

5. L. Galluzzi, F. Pietrocola, B. Levine, G. Kroemer, Metabolic control of autophagy. *Cell* **159**, 1263–1276 (2014).

6. N. Mizushima, D. J. Klionsky, Protein turnover via autophagy: implications for metabolism. *Annu Rev Nutr* **27**, 19–40 (2007).

7. V. Deretic, Autophagy in inflammation, infection, and immunometabolism. *Immunity* **54**, 437–453 (2021).

8. L. Galluzzi, T. Yamazaki, G. Kroemer, Linking cellular stress responses to systemic homeostasis. *Nat Rev Mol Cell Biol* **19**, 731–745 (2018).

9. B. Levine, G. Kroemer, Biological Functions of Autophagy Genes: A Disease Perspective. *Cell* **176**, 11–42 (2019).

10. J. M. Bravo-San Pedro, *et al.*, Acyl-CoA-Binding Protein Is a Lipogenic Factor that Triggers Food Intake and Obesity. *Cell Metab* **30**, 754-767.e9 (2019).

11. M. Kitada, D. Koya, Autophagy in metabolic disease and ageing. *Nat Rev Endocrinol* **17**, 647–661 (2021).

12. J. O. Pyo, *et al.*, Overexpression of Atg5 in mice activates autophagy and extends lifespan. *Nat Commun* **4** (2013).

13. Á. F. Fernández, *et al.*, Disruption of the beclin 1-BCL2 autophagy regulatory complex promotes longevity in mice. *Nature* **558**, 136–140 (2018).

14. Y. X. Lu, *et al.*, A TORC1-histone axis regulates chromatin organisation and non-canonical induction of autophagy to ameliorate ageing. *Elife* **10** (2021).

15. M. Hansen, D. C. Rubinsztein, D. W. Walker, Autophagy as a promoter of longevity: insights from model organisms. *Nat Rev Mol Cell Biol* **19**, 579–593 (2018).

16. T. Eisenberg, *et al.*, Cardioprotection and lifespan extension by the natural polyamine spermidine. *Nat Med* **22**, 1428–1438 (2016).

17. N. Tavernarakis, A. Pasparaki, E. Tasdemir, M. C. Maiuri, G. Kroemer, The effects of p53 on whole organism longevity are mediated by autophagy. *Autophagy* **4**, 870–873 (2008).

18. A. Meléndez, *et al.*, Autophagy genes are essential for dauer development and life-span extension in C. elegans. *Science* **301**, 1387–1391 (2003).

19. F. Madeo, D. Carmona-Gutierrez, S. J. Hofer, G. Kroemer, Caloric Restriction Mimetics against Age-Associated Disease: Targets, Mechanisms, and Therapeutic Potential. *Cell Metab* **29**, 592–610 (2019).

20. M. Allaire, P. E. Rautou, P. Codogno, S. Lotersztajn, Autophagy in liver diseases: Time for translation? *J Hepatol* **70**, 985–998 (2019).

21. Y. Hazari, J. M. Bravo-San Pedro, C. Hetz, L. Galluzzi, G. Kroemer, Autophagy in hepatic adaptation to stress. *J Hepatol* **72**, 183–196 (2020).

22. S. Sciarretta, Y. Maejima, D. Zablocki, J. Sadoshima, The Role of Autophagy in the Heart. *Annu Rev Physiol* **80**, 1–26 (2018).

23. A. C. Racanelli, A. M. K. Choi, M. E. Choi, Autophagy in chronic lung disease. *Prog Mol Biol Transl Sci* **172**, 135–156 (2020).

24. M. E. Choi, Autophagy in Kidney Disease. *Annu Rev Physiol* **82**, 297–322 (2020).

25. D. J. Klionsky, *et al.*, Autophagy in major human diseases. *EMBO J* **40** (2021).

26. Z. Lin, *et al.*, Adiponectin protects against acetaminophen-induced mitochondrial dysfunction and acute liver injury by promoting autophagy in mice. *J Hepatol* **61**, 825–831 (2014).

27. Y. Shen, *et al.*, Decreased Hepatocyte Autophagy Leads to Synergistic IL-1β and TNF Mouse Liver Injury and Inflammation. *Hepatology* **72**, 595–608 (2020).

28. X. Chao, W. X. Ding, Role and mechanisms of autophagy in alcohol-induced liver injury. *Adv Pharmacol* **85**, 109–131 (2019).

29. L. Galluzzi, J. M. Bravo-San Pedro, B. Levine, D. R. Green, G. Kroemer, Pharmacological modulation of autophagy: therapeutic potential and persisting obstacles. *Nat Rev Drug Discov* **16**, 487–511 (2017).

30. I. Dikic, Z. Elazar, Mechanism and medical implications of mammalian autophagy. *Nat Rev Mol Cell Biol* **19**, 349–364 (2018).

31. W. C. Chiang, *et al.*, High-Throughput Screens To Identify Autophagy Inducers That Function by Disrupting Beclin 1/Bcl-2 Binding. *ACS Chem Biol* **13**, 2247–2260 (2018).

32. M. I. Capurro, *et al.*, VacA generates a protective intracellular reservoir for Helicobacter pylori that is eliminated by activation of the lysosomal calcium channel TRPML1. *Nat Microbiol* **4**, 1411–1423 (2019).

33. W. F. Loomis, M. M. Behrens, M. E. Williams, C. Anjard, Pregnenolone sulfate and cortisol induce secretion of acyl-CoA-binding protein and its conversion into endozepines from astrocytes. *J Biol Chem* **285**, 21359–21365 (2010).

34. A. Joseph, *et al.*, Metabolic and psychiatric effects of acyl coenzyme A binding protein (ACBP)/diazepam binding inhibitor (DBI). *Cell Death Dis* **11** (2020).

35. A. Joseph, *et al.*, Effects of acyl-coenzyme A binding protein (ACBP)/diazepam-binding inhibitor (DBI) on body mass index. *Cell Death Dis* **12** (2021).

36. S. Venkatesh, *et al.*, Mitochondrial LonP1 protects cardiomyocytes from ischemia/reperfusion injury in vivo. *J Mol Cell Cardiol* **128**, 38–50 (2019).

37. O. Motiño, *et al.*, Protective Role of Hepatocyte Cyclooxygenase-2 Expression Against Liver Ischemia–Reperfusion Injury in Mice. *Hepatology* **70** (2019).

38. O. Motiño, *et al.*, Cyclooxygenase-2 expression in hepatocytes attenuates non-alcoholic steatohepatitis and liver fibrosis in mice. *Biochimica et Biophysica Acta - Molecular Basis of Disease* **1862** (2016).

39. C. G. Tag, *et al.*, Bile Duct Ligation in Mice: Induction of Inflammatory Liver Injury and Fibrosis by Obstructive Cholestasis. *JoVE (Journal of Visualized Experiments)* **96**, e52438 (2015).

40. S. N. Kim, *et al.*, Dose-response Effects of Bleomycin on Inflammation and Pulmonary Fibrosis in Mice. *Toxicological Research* **26**, 217 (2010).

41. N. Mizushima, A. Yamamoto, M. Matsui, T. Yoshimori, Y. Ohsumi, In vivo analysis of autophagy in response to nutrient starvation using transgenic mice expressing a fluorescent autophagosome marker. *Mol Biol Cell* **15**, 1101–1111 (2004).

42. J. Haspel, *et al.*, Characterization of macroautophagic flux in vivo using a leupeptin-based assay. *Autophagy* **7**, 629–642 (2011).

43. S. Suzuki, L. H. Toledo-Pereyra, F. J. Rodriguez, D. Cejalvo, Neutrophil infiltration as an important factor in liver ischemia and reperfusion injury. Modulating effects of FK506 and cyclosporine. *Transplantation* **55**, 1265–1271 (1993).

44. K. L. Cook, *et al.*, Hydroxychloroquine inhibits autophagy to potentiate antiestrogen responsiveness in ER+ breast cancer. *Clin Cancer Res* **20**, 3222–3232 (2014).

45. A. Shirakabe, *et al.*, Evaluating mitochondrial autophagy in the mouse heart. *J Mol Cell Cardiol* **92**, 134–139 (2016).

46. L. Montégut, *et al.*, Immunization of mice with the self-peptide ACBP coupled to keyhole limpet hemocyanin. *STAR Protoc* **3**, 101095 (2022).

47. P. Wulff, *et al.*, From synapse to behavior: rapid modulation of defined neuronal types with engineered GABAA receptors. *Nat Neurosci* **10**, 923–929 (2007).

48. A. Mohs, *et al.*, Hepatocyte-specific NRF2 activation controls fibrogenesis and carcinogenesis in steatohepatitis. *J Hepatol* **74**, 638–648 (2021).

49. I. R. Schlaepfer, M. Joshi, CPT1A-mediated Fat Oxidation, Mechanisms, and Therapeutic Potential. *Endocrinology* **161** (2020).

50. G. Serviddio, *et al.*, Oxidation of Hepatic Carnitine Palmitoyl Transferase-I (CPT-I) Impairs Fatty Acid Beta-Oxidation in Rats Fed a Methionine-Choline Deficient Diet. *PLoS ONE* **6**, 24084 (2011).

51. A. Montagner, *et al.*, Liver PPARα is crucial for whole-body fatty acid homeostasis and is protective against NAFLD. *Gut* **65**, 1202–1214 (2016).

52. Y. Nakade, *et al.*, Conophylline inhibits non-alcoholic steatohepatitis in mice. *PLoS One* **12** (2017).

53. Á. F. Fernández, *et al.*, Autophagy couteracts weight gain, lipotoxicity and pancreatic β-cell death upon hypercaloric pro-diabetic regimens. *Cell Death Dis* **8** (2017).

54. E. E. Powell, V. W. S. Wong, M. Rinella, Non-alcoholic fatty liver disease. *Lancet* **397**, 2212–2224 (2021).

55. R. Brea, *et al.*, PGE2 induces apoptosis of hepatic stellate cells and attenuates liver fibrosis in mice by downregulating miR-23a-5p and miR-28a-5p. *Biochimica et Biophysica Acta (BBA) - Molecular Basis of Disease* **1864**, 325–337 (2018).

56. J. M. Bravo-San Pedro, *et al.*, Cell-autonomous, paracrine and neuroendocrine feedback regulation of autophagy by DBI/ACBP (diazepam binding inhibitor, acyl-CoA binding protein): the obesity factor. *Autophagy* **15**, 2036–2038 (2019).

57. N. Charmpilas, *et al.*, Acyl-CoA-binding protein (ACBP): a phylogenetically conserved appetite stimulator. *Cell Death Dis* **11** (2020).

58. G. Anagnostopoulos, *et al.*, Correction: An obesogenic feedforward loop involving PPARγ, acyl-CoA binding protein and GABA receptor. *Cell Death & Disease 2022 13:5* **13**, 1–1 (2022).

59. D. Neess, *et al.*, Epidermal Acyl-CoA-binding protein is indispensable for systemic energy homeostasis. *Mol Metab* **44** (2021).

60. A. M. Thomas, F. Asnicar, G. Kroemer, N. Segata, Genes Encoding Microbial Acyl Coenzyme A Binding Protein/Diazepam-Binding Inhibitor Orthologs Are Rare in the Human Gut Microbiome and Show No Links to Obesity. *Appl Environ Microbiol* **87**, 1–11 (2021).

61. D. Neess, S. Bek, H. Engelsby, S. F. Gallego, N. J. Færgeman, Long-chain acyl-CoA esters in metabolism and signaling: Role of acyl-CoA binding proteins. *Prog Lipid Res* **59**, 1–25 (2015).

62. M. Shamalnasab, *et al.*, HIF-1-dependent regulation of lifespan in Caenorhabditis elegans by the acyl-CoA-binding protein MAA-1. *Aging* **9**, 1745–1769 (2017).

63. P. Fabrizio, *et al.*, Genome-wide screen in Saccharomyces cerevisiae identifies vacuolar protein sorting, autophagy, biosynthetic, and tRNA methylation genes involved in life span regulation. *PLoS Genet* **6**, 1–14 (2010).

64. S. Xiao, M. L. Chye, The Arabidopsis thaliana ACBP3 regulates leaf senescence by modulating phospholipid metabolism and ATG8 stability. *Autophagy* **6** (2010).

65. L. Bejarano, M. J. C. Jordão, J. A. Joyce, Therapeutic Targeting of the Tumor Microenvironment. *Cancer Discov* **11**, 933–959 (2021).

66. P. Sharma, J. P. Allison, Immune checkpoint targeting in cancer therapy: toward combination strategies with curative potential. *Cell* **161**, 205–214 (2015).

Figures Legends

Figure 1. Neutralization of ACBP/DBI activates autophagy flux and attenuates ischemia/reperfusion injury *in vivo*.

A-B C57BL/6 mice were injected intraperitoneally (i.p.) with a monoclonal antibody (mAb) neutralizing ACBP/DBI (α-DBI) or control isotype (IgG) (2.5 µg/g i.p. 6 and 2 hours before sacrifice) and the autophagy flux inhibitor leupeptin (Leu, 30 mg/kg, 2 hours before sacrifice). Representative Western blot **(A)** and densitometric quantification **(B)** from the liver tissues, upon normalization (relative expression, RE) to the LC3B II / I ratio (n=6 mice per group).

C-D Representative confocal images **(C)** and LC3 dots quantification (counts / 100 mm^2) **(D)** from livers recovered from LC3-GFP transgenic mice after i.p. injection of α-DBI or IgG (2.5 µg/g, 4 hours before sacrifice) (n=5 mice per group).

E-I Liver injury produced by ischemia/reperfusion (IR) for 90 min /4 hours. Schematic representation **(E)** of the damage induced by hepatic IR in mice pre-treated with i.p. injection of α-DBI or IgG (2.5 µg/g) and HCQ (50 mg/kg) for 4 hours and just before IR. Representative images of hematoxylin/eosin/safranin-stained (HES) liver section **(F)** from mice pre-treated with α-DBI or IgG and HCQ after sham operation or IR. Asterisk, arrows, and arrowheads indicate necrotic areas, vacuolization, and vascular congestion, respectively. The liver injury **(G)** was assessed by histological examination. ALT (**H**) and AST transaminase activity (**I**) in plasma was analyzed by means of a colorimetric assay (n=4-11 mice per group).

Results are displayed as means ± SEM. For statistical analyses, *p* values were calculated by ANOVA test **(B, G-I)** or two-tailed unpaired Student's t test **(D)**.

Figure 2. ACBP/DBI Neutralization activates autophagy/mitophagy flux and reduces cardiac damage in mice.

A-B α-DBI or IgG (2.5 µg/g 6 and 2 hours before sacrifice) and leupeptin (30 mg/kg, 2 hours before sacrifice) were injected i.p. in C57BL/6 mice. Immunoblot of LC3B **(A)** and densitometric quantification **(B)** from heart extracts (n=6 mice per group).

C-D Mito-Keima transgenic mice were injected twice with IgG or α-DBI i.p. 6 and 2 hours before sacrifice (2.5 µg/g). Representative confocal microscopy images **(C)** and quantification of signals **(D)** (n=3 mice per group).

E-G *Wt* (*Atg7*$^{fl/fl}$, αMHC *Cre*$^{-}$) and homozygous *Atg7*$^{-/-}$ (*Atg7*$^{fl/fl}$, αMHC *Cre*$^{+}$) mice were subjected to 3 hours of ischemia **(E)**. Mice were injected with IgG or α-DBI i.p. 4 hours before ischemia and just before ischemia. Representative images of left ventricular myocardial sections after Alcian blue and TTC (2,3,5-Triphenyltetrazolium chloride) staining **(F)** and quantification of the infarction size *versus* area-at-risk of myocardial damage **(G)** (n=4-6 mice per group).

Results are displayed as means ± SEM. For statistical analyses, *p* values were calculated by ANOVA test **(B, G)** or two-tailed unpaired Student's t test **(D)**.

Figure 3. ACBP/DBI neutralization and ablation protect against MCD-induced hepatic steatosis, inflammation, and ballooning *in vivo*.

A Experimental strategy of the NASH injury induced by MCD for 4 weeks (control with regular chow diet, RCD). C57BL/6 mice were injected i.p. with α-DBI or IgG (2.5 µg/g) one day before the beginning of the diet and every week during the diet (left panel). Inducible whole-body knockout of *Acbp/Dbi* (*Dbi*$^{-/-}$) or control (*Wt*) mice were injected i.p. with tamoxifen daily for 5 days (right panel).

B-H α-DBI reduces the hepatic damage produced by MCD diet through autophagy activation. Representatives immunoblot **(B)** and densitometric analysis of the ratio LC3B II / I **(C)** and p62 **(D)** normalized against GAPDH (both expressed as relative expression, RE) from liver extracts. Hepatic HES images **(E)** and NAFLD activity score (measured as sum of steatosis, inflammation, and ballooning score) **(F)**, and ALT **(G)** and AST activity **(H)** in plasma from mice treated with α-DBI or IgG. (n=3-10 mice per group).

I-O Genetic ablation of ACBP/DBI reverts derived- NASH diet nocuous effect by autophagy activation. Western blots **(I)** and densitometric analysis of p62 **(J)**, LC3B **(K)** and DBI from liver extracts. Histological pictures from liver HES staining **(L)**, NAFLD activity score **(M)** and hepatic damaged measured by plasmatic levels of ALT **(N)** and AST activity **(O)** from *Dbi*$^{-/-}$ and *Wt* mice (n=5-16 mice per group).

Asterisk, arrows, and arrowheads indicate inflammation foci, macro-steatosis, and micro-steatosis vesicular, respectively.

Data are displayed as means ± SEM. Statistical analyses (*p* value) were calculated by ANOVA test.

Figure 4. Metabolic and pro-autophagic effects of α-DBI in the context of MCD.

A Heatmap clustered by Euclidean distance of changes in liver metabolite concentrations depicted as $\log^2$ (fold change) (FC) in C57BL/6 mice injected with IgG or α-DBI after MCD (left panel) (n=3 to 9 mice per group). All carnitines are depicted in the right panel.

B-D Expression of b-oxidation-relevant enzymes. Representative Western Blot (top) and densitometric quantification (bottom) of CPT1A after **(B)** (n=5-8 mice in each group). mRNA levels of *Cpt1a* **(C)** and *Ppara* **(D)** analyzed by RT-qPCR (n=4-8 mice per group).

E-L Comparison of anti-NASH effects of α-DBI in Wt and autophagy-deficiency (*Atg4b*$^{-/-}$) mice under MCD. Representative immunoblots of autophagy markers such as ATG4B, p62 and LC3B **(E)**, and densitometric analysis of p62 **(F)** and LC3B **(G)**. Representative histological images **(H)** and NAFLD activity scores **(I)**. ALT **(J)** and AST **(K)** were measured in plasma (n=5-8 mice per

group). Expression of genes involved in inflammation (*Cd68, F480, Il1b, Il6, Mcp1, Nrlp3, Tnfa*), antioxidant response (*Cat, Hmox1, Nrf2, Gpx, Gsr, Sod1, Sod2*), and β-oxidation (*Cpt1a, Pgc1a, Ppara*) were measured by RT-qPCR and represented in volcano plots **(L)** (n=3-8 mice per group). Asterisks, arrows, and arrowheads show inflammation foci, macro-steatosis and micro-steatosis vesicular, respectively.

Results are displayed as means ± SEM. For statistical analyses, *p* values were calculated by ANOVA test **(B, D, F-G, J-K)**, Kruskal-Wallis test **(C, I)** or two-tailed unpaired Student's t test **(L).**

Figure 5. ACBP/DBI neutralization accelerates the recovery from NASH.

A-G α-DBI reduces hepatic damage (steatosis, inflammation, and ballooning), ameliorating recovery. Mice were fed MCD for 4 weeks to induce NASH and then were fed RCD (reversion, R) for 4 days. α-DBI or IgG was injected i.p. twice, one day before switch MCD to RCD and one day before sacrifice. Representative pictures of HES staining **(A)**, NAFLD activity score **(B)**, ALT and AST transaminases activity (**C** and **D** respectively) were analyzed in plasma (n=3-10 mice per group). Volcano plots of genes implicated in inflammation (*Cd68, F480, Il1b, Il6, Tnfa*), antioxidant response (*Cat, Hmox1, Nrf2, Gpx, Gsr, Sod1, Sod2*), and b-oxidation (*Cpt1a, Pgc1a, Ppara*) were measured by RT-qPCR. The comparation between MCD IgG (n=6) and RCD IgG (n=5-6), R IgG (n=7-8) and MCD IgG, and R α-DBI (n=7-8) and R IgG are shown in **E**, **F** and **G**, respectively.

H-I Heatmap clustered by Euclidean distance **(H)** of changes in liver metabolite concentrations depicted as log2 fold change (FC) in C57BL/6 mice injected with IgG or α-DBI (top panel) All carnitines are shown in the bottom panel (**H**) and quantified **(I)** (n=12 to 25 mice per group).

J-N The inhibition of autophagy or β-oxidation attenuates the beneficial effects of α-DBI in mice. Representative images of HES staining **(J-K, M)** and NAFLD activity score (**L, N**) from several groups (n=5-10 mice per condition).

Asterisks show inflammation foci.

Results are displayed as means ± SEM. Statistical analyses (*p* values) were performed by ANOVA test **(B-C, I, N)**, two-tailed unpaired Student's t test **(E-G)** or Kruskal-Wallis test **(L).**

Figure 6. Neutralization of ACBP/DBI attenuates fibrosis induced by chronic liver damage.

A-D C57BL/6 mice were subjected to bile duct ligation (BDL) for 2 weeks. Mice were injected with 2.5 µg/g IgG or α-DBI i.p. 4 hours and 1 h before BDL, and twice per week during BDL Representative images from hepatic Picro-Sirius Red staining **(A)**. Fibrosis scores **(B)**, ALT activity **(C)** and bilirubin levels **(D)** were measured (n=5-10 mice per group).

E-I C57BL/6 mice were injected i.p. with 2.5 µg/g α-DBI or IgG weekly and 1.6 ml/kg CCl_4 twice per week for 9 weeks. Additional group was treated with 50 mg/kg/day of HCQ for 4 last weeks of CCl_4 **(E)**. Representative Picro-Sirius Red stained paraffin-embedded sections **(F)**, the quantification of

fibrosis stage **(G)** and plasma ALT **(H)** are shown (n=5-14 mice per group). Analysis of genes involved in fibrosis, inflammation (including macrophages markers), and oxidative stress. Heatmap clustered by Euclidean distance of changes in mRNA levels depicted as log^2 (fold change) in C57BL/6 mice injected with IgG or α-DBI plus HCQ after CCl_4 **(I)** (n=3-10 mice per group).
Results are displayed as means ± SEM. For statistical analyses, *p* values were calculated by ANOVA test **(B-D)** or Kruskal-Wallis test **(G-I)**.

Figure 7. α-DBI enhanced the recovery of liver fibrosis in an autophagy-dependent fashion.
A-E Experimental strategy for fibrosis reversion. Mice received CCl_4 for 9 weeks and then were treated with vehicle (oil) for 4 weeks of reversion (R). 2.5 µg/g IgG or α-DBI was injected i.p. one day before reversion and weekly for R **(A)**. Representative images of Picro-Sirius Red stained paraffin-embedded sections **(B)**, quantification of fibrosis stage **(C)**, plasmatic ALT activity **(D)** and hydroxyproline levels **(E)** (n=4-12 mice per group).
Results are displayed as means ± SEM. For statistical analyses, *p* values were calculated by ANOVA test **(C-E)**.

Figure 8. ACBP/DBI neutralization attenuates lung fibrosis induced by bleomycin.
A-E Lung fibrosis was induced by intratracheal injection of one dose of 2 mg/kg bleomycin (Bleo) for 18 days in C57BL/6 mice. 2.5 µg/g α-DBI or IgG was injected each weak **(A)**. Histological section of Picro-Sirius Red/Fast Green staining **(B)** and damage/fibrosis Ashcroft score **(C)** were shown. Volcano plots of genes related with fibrosis (*Acta2, Desmin, Col1a1, Col1a2, Col6a1, Col6a2, Col6a3, Pdfga, Pdgfb, Pdgfra, Pdgfrb*, *Vimentin*), inflammation (*Cd68, F480, Il1b, Il6, Mcp1, Nrlp3, Tnfa*), and antioxidant response (*Cat, Hmox1, Nrf2, Gpx, Gsr, Sod1, Sod2*) were measured by RT-qPCR. The comparisons between Bleo IgG (n=6-7) *versus* Ctrl IgG (n=3) **(D)** and Bleo α-DBI (n=7-9) *versus* Bleo IgG **(E)** are represented.
Results are displayed as means ± SEM. For statistical analyses, *p* values were calculated by Kruskal-Wallis test **(C)** and two-tailed unpaired Student's t test **(D-E)**.

Figure 9. Summary scheme of ACBP/DBI neutralization in several organs. ACBP/DBI neutralization protects against hepatic (Acute, NASH, and Fibrosis), heart (Ischemia) and pulmonary (Fibrosis) damage through autophagy activation. This protection is due to the suppression of the cell loss, inflammation, and fibrosis. The inhibition of autophagy by hydroxychloroquine treatment, or *Atg4b*/*Atg7* genetic deficiency reverts the beneficial effect of ACBP/DBI neutralization. The proposed model was created with BioRender.com.

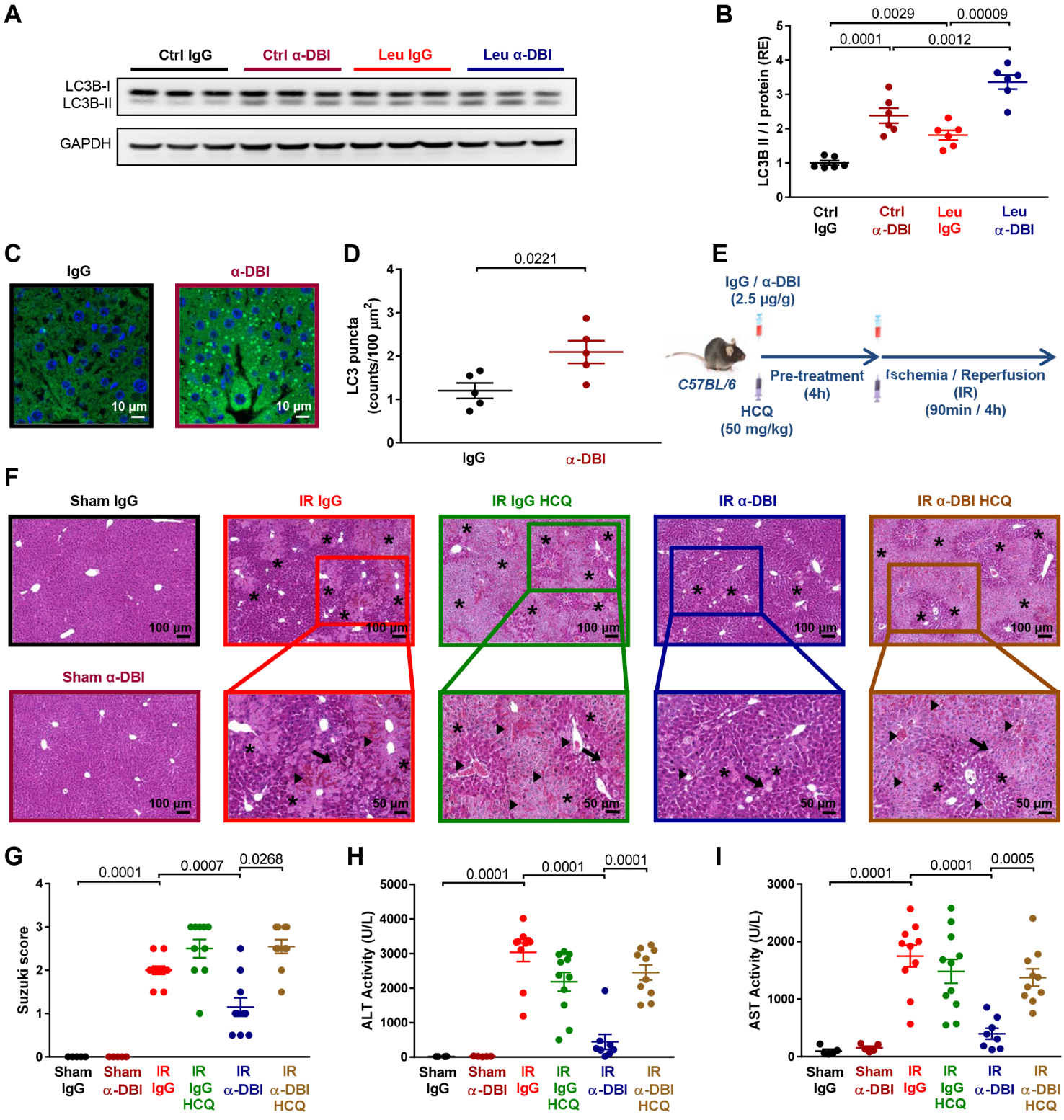
A
Ctrl IgG
Ctrl α-DBI
Leu IgG
Leu α-DBI
LC3B-I
LC3B-II
GAPDH
B
0.0029
0.00009
0.0001
0.0012
LC3B II / I protein (RE)
Ctrl IgG
Ctrl α-DBI
Leu IgG
Leu α-DBI
C
IgG
α-DBI
10 μm
D
0.0221
LC3 puncta (counts/100 μm²)
IgG
α-DBI
E
IgG / α-DBI (2.5 μg/g)
C57BL/6
Pre-treatment (4h)
Ischemia / Reperfusion (IR) (90min / 4h)
HCQ (50 mg/kg)
F
Sham IgG
IR IgG
IR IgG HCQ
IR α-DBI
IR α-DBI HCQ
Sham α-DBI
100 μm
50 μm
G
0.0001
0.0007
0.0268
Suzuki score
Sham IgG
Sham α-DBI
IR IgG
IR IgG HCQ
IR α-DBI
IR α-DBI HCQ
H
0.0001
0.0001
0.0001
ALT Activity (U/L)
I
0.0001
0.0001
0.0005
AST Activity (U/L)

Figure 1

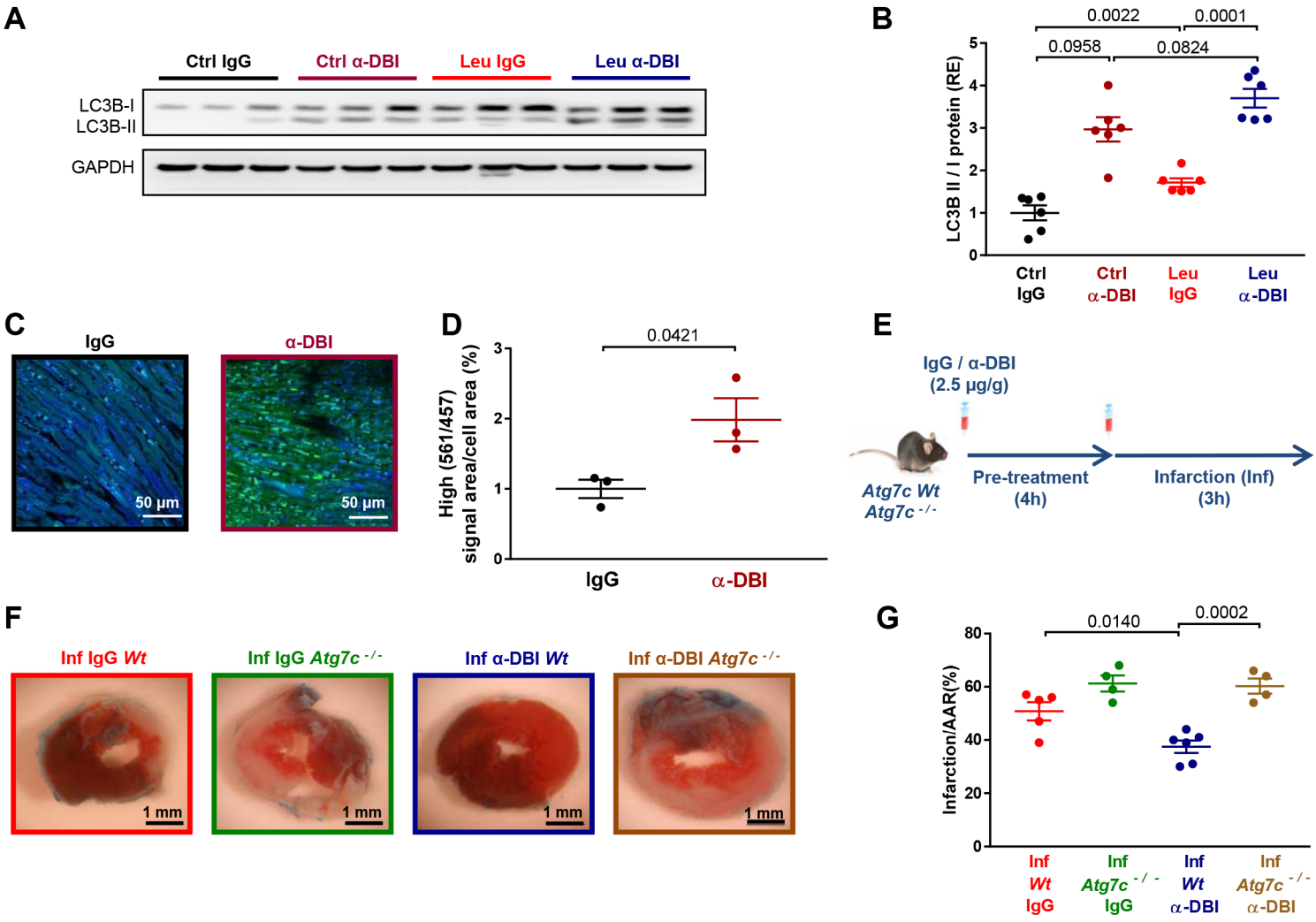
A
Ctrl IgG
Ctrl α-DBI
Leu IgG
Leu α-DBI
LC3B-I
LC3B-II
GAPDH
B
0.0022
0.0001
0.0958
0.0824
LC3B II / I protein (RE)
Ctrl IgG
Ctrl α-DBI
Leu IgG
Leu α-DBI
C
IgG
α-DBI
50 µm
50 µm
D
0.0421
High (561/457) signal area/cell area (%)
IgG
α-DBI
E
IgG / α-DBI (2.5 µg/g)
Atg7c Wt
Atg7c -/-
Pre-treatment (4h)
Infarction (Inf) (3h)
F
Inf IgG Wt
Inf IgG Atg7c -/-
Inf α-DBI Wt
Inf α-DBI Atg7c -/-
1 mm
1 mm
1 mm
1 mm
G
0.0140
0.0002
Infarction/AAR(%)
Inf Wt IgG
Inf Atg7c -/- IgG
Inf Wt α-DBI
Inf Atg7c -/- α-DBI

Figure 2

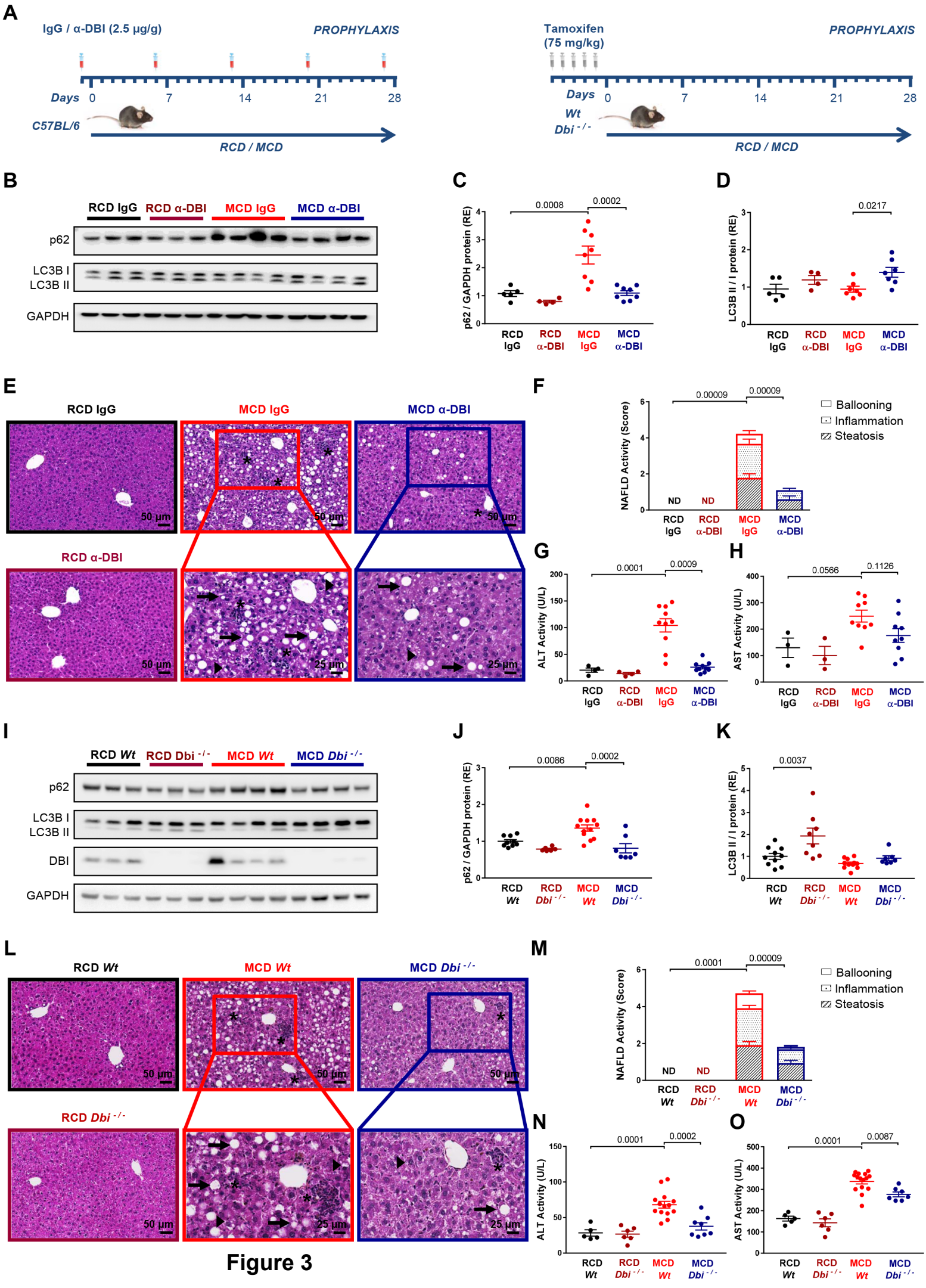
A
IgG / α-DBI (2.5 µg/g)
PROPHYLAXIS
Days 0 7 14 21 28
C57BL/6
RCD / MCD
Tamoxifen (75 mg/kg)
PROPHYLAXIS
Days 0 7 14 21 28
Wt
Dbi -/-
RCD / MCD
B
RCD IgG
RCD α-DBI
MCD IgG
MCD α-DBI
p62
LC3B I
LC3B II
GAPDH
C
p62 / GAPDH protein (RE)
0.0008
0.0002
RCD IgG
RCD α-DBI
MCD IgG
MCD α-DBI
D
LC3B II / I protein (RE)
0.0217
E
RCD IgG
MCD IgG
MCD α-DBI
RCD α-DBI
50 µm
25 µm
F
NAFLD Activity (Score)
0.00009
0.00009
ND
Ballooning
Inflammation
Steatosis
G
ALT Activity (U/L)
0.0001
0.0009
H
AST Activity (U/L)
0.0566
0.1126
I
RCD Wt
RCD Dbi -/-
MCD Wt
MCD Dbi -/-
p62
LC3B I
LC3B II
DBI
GAPDH
J
p62 / GAPDH protein (RE)
0.0086
0.0002
K
LC3B II / I protein (RE)
0.0037
L
RCD Wt
MCD Wt
MCD Dbi -/-
RCD Dbi -/-
50 µm
25 µm
M
NAFLD Activity (Score)
0.0001
0.00009
ND
Ballooning
Inflammation
Steatosis
N
ALT Activity (U/L)
0.0001
0.0002
O
AST Activity (U/L)
0.0001
0.0087

Figure 3

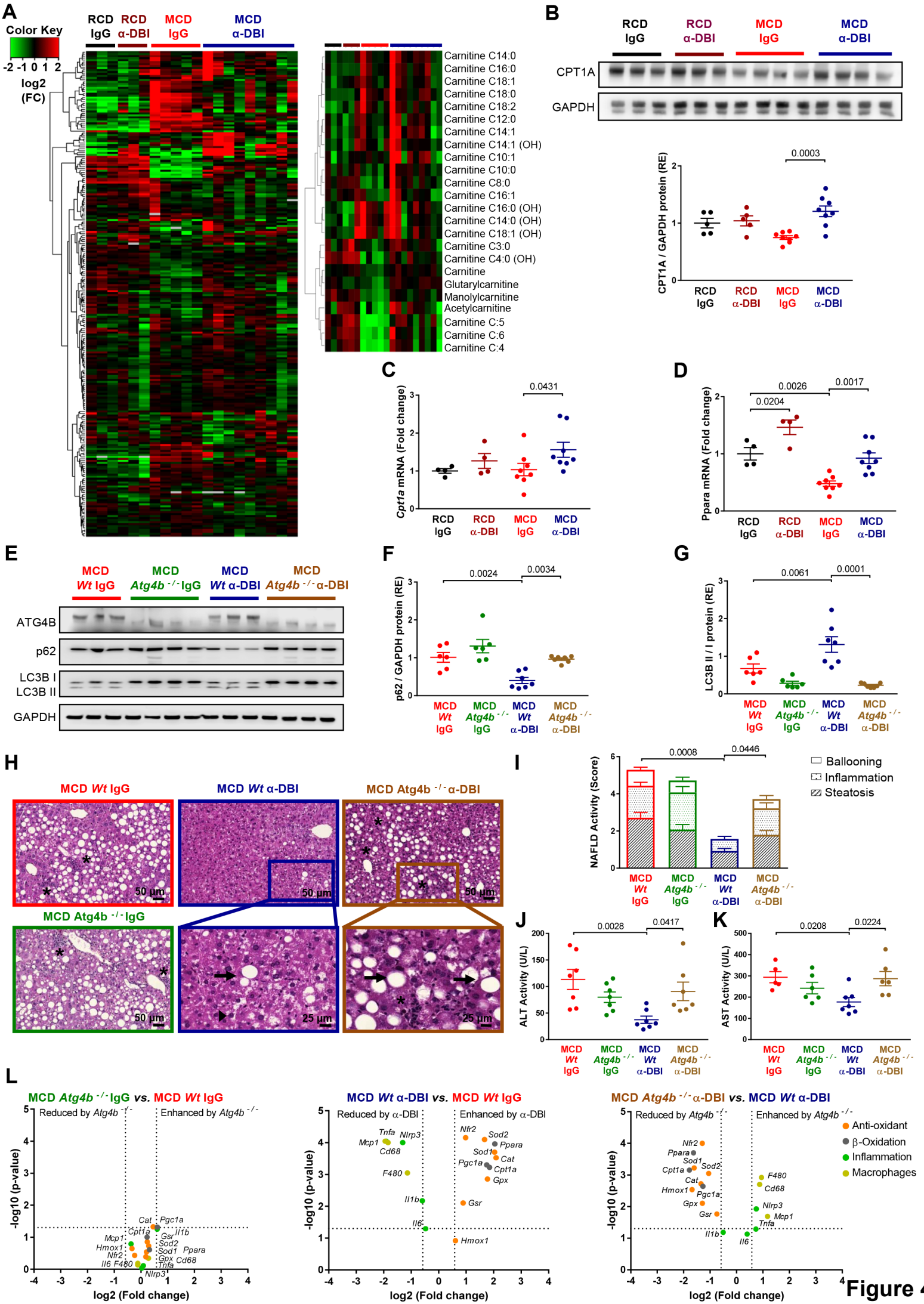
A
Color Key
-2 -1 0 1 2
log2 (FC)
RCD IgG
RCD α-DBI
MCD IgG
MCD α-DBI
Carnitine C14:0
Carnitine C16:0
Carnitine C18:1
Carnitine C18:0
Carnitine C18:2
Carnitine C12:0
Carnitine C14:1
Carnitine C14:1 (OH)
Carnitine C10:1
Carnitine C10:0
Carnitine C8:0
Carnitine C16:1
Carnitine C16:0 (OH)
Carnitine C14:0 (OH)
Carnitine C18:1 (OH)
Carnitine C3:0
Carnitine C4:0 (OH)
Carnitine
Glutarylcarnitine
Manolylcarnitine
Acetylcarnitine
Carnitine C:5
Carnitine C:6
Carnitine C:4
B
CPT1A
GAPDH
CPT1A / GAPDH protein (RE)
0.0003
C
Cpt1a mRNA (Fold change)
0.0431
D
Ppara mRNA (Fold change)
0.0026
0.0017
0.0204
E
MCD Wt IgG
MCD Atg4b -/- IgG
MCD Wt α-DBI
MCD Atg4b -/- α-DBI
ATG4B
p62
LC3B I
LC3B II
GAPDH
F
p62 / GAPDH protein (RE)
0.0024
0.0034
G
LC3B II / I protein (RE)
0.0061
0.0001
H
MCD Wt IgG
MCD Wt α-DBI
MCD Atg4b -/- α-DBI
MCD Atg4b -/- IgG
50 μm
25 μm
I
NAFLD Activity (Score)
0.0008
0.0446
Ballooning
Inflammation
Steatosis
J
ALT Activity (U/L)
0.0028
0.0417
K
AST Activity (U/L)
0.0208
0.0224
L
MCD Atg4b -/- IgG vs. MCD Wt IgG
Reduced by Atg4b -/-
Enhanced by Atg4b -/-
MCD Wt α-DBI vs. MCD Wt IgG
Reduced by α-DBI
Enhanced by α-DBI
MCD Atg4b -/- α-DBI vs. MCD Wt α-DBI
Reduced by Atg4b -/-
Enhanced by Atg4b -/-
Anti-oxidant
β-Oxidation
Inflammation
Macrophages
-log10 (p-value)
log2 (Fold change)

Figure 4

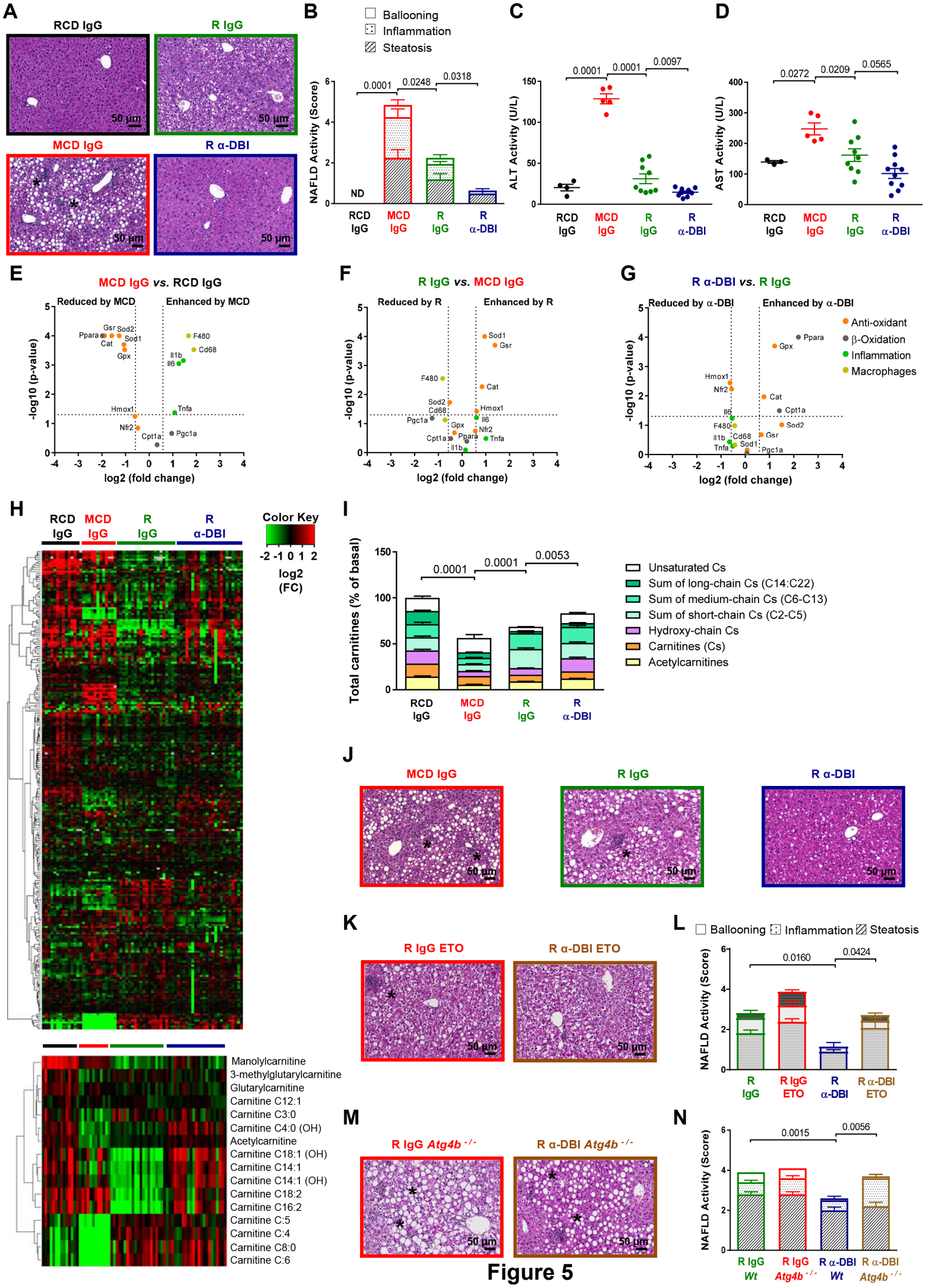
A
RCD IgG
R IgG
MCD IgG
R α-DBI
50 μm
B
Ballooning
Inflammation
Steatosis
NAFLD Activity (Score)
ND
0.0001
0.0248
0.0318
RCD IgG
MCD IgG
R IgG
R α-DBI
C
ALT Activity (U/L)
0.0001
0.0001
0.0097
D
AST Activity (U/L)
0.0272
0.0209
0.0565
E
MCD IgG vs. RCD IgG
Reduced by MCD
Enhanced by MCD
-log10 (p-value)
log2 (fold change)
Gsr
Sod2
Pparα
Cat
Sod1
Gpx
F480
Cd68
Il1b
Il6
Tnfa
Hmox1
Nfr2
Cpt1a
Pgc1a
F
R IgG vs. MCD IgG
Reduced by R
Enhanced by R
G
R α-DBI vs. R IgG
Reduced by α-DBI
Enhanced by α-DBI
Anti-oxidant
β-Oxidation
Inflammation
Macrophages
H
RCD IgG
MCD IgG
R IgG
R α-DBI
Color Key
-2 -1 0 1 2
log2 (FC)
Manolylcarnitine
3-methylglutarylcarnitine
Glutarylcarnitine
Carnitine C12:1
Carnitine C3:0
Carnitine C4:0 (OH)
Acetylcarnitine
Carnitine C18:1 (OH)
Carnitine C14:1
Carnitine C14:1 (OH)
Carnitine C18:2
Carnitine C16:2
Carnitine C:5
Carnitine C:4
Carnitine C8:0
Carnitine C:6
I
Total carnitines (% of basal)
0.0001
0.0001
0.0053
Unsaturated Cs
Sum of long-chain Cs (C14:C22)
Sum of medium-chain Cs (C6-C13)
Sum of short-chain Cs (C2-C5)
Hydroxy-chain Cs
Carnitines (Cs)
Acetylcarnitines
J
MCD IgG
R IgG
R α-DBI
K
R IgG ETO
R α-DBI ETO
L
Ballooning
Inflammation
Steatosis
NAFLD Activity (Score)
0.0160
0.0424
R IgG
R IgG ETO
R α-DBI
R α-DBI ETO
M
R IgG Atg4b -/-
R α-DBI Atg4b -/-
N
NAFLD Activity (Score)
0.0015
0.0056
R IgG Wt
R IgG Atg4b -/-
R α-DBI Wt
R α-DBI Atg4b -/-

Figure 5

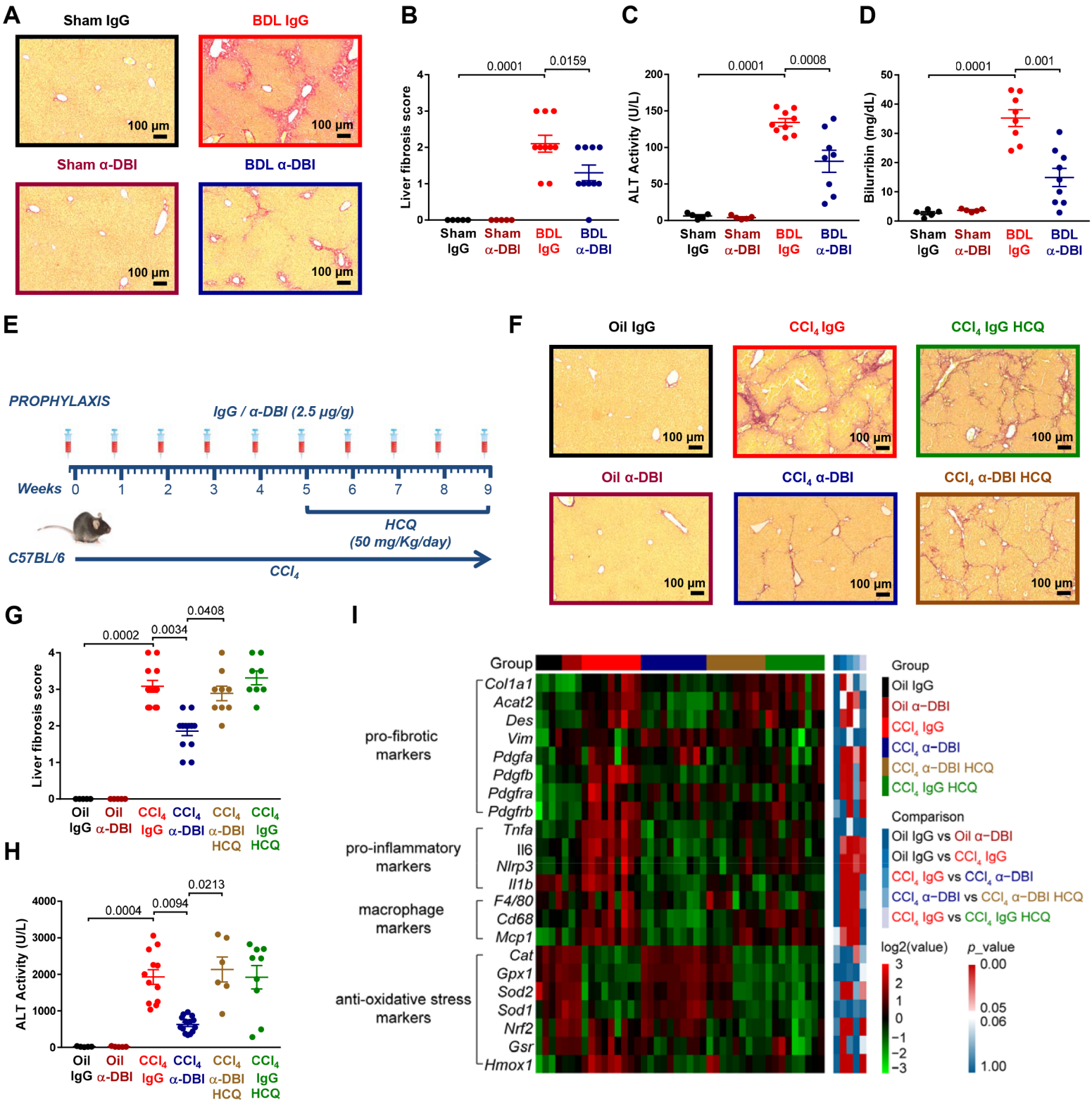
A
Sham IgG
BDL IgG
Sham α-DBI
BDL α-DBI
100 μm
B
Liver fibrosis score
0.0001
0.0159
C
ALT Activity (U/L)
0.0001
0.0008
D
Bilurribin (mg/dL)
0.0001
0.001
Sham IgG
Sham α-DBI
BDL IgG
BDL α-DBI
E
PROPHYLAXIS
IgG / α-DBI (2.5 μg/g)
Weeks 0 1 2 3 4 5 6 7 8 9
HCQ
(50 mg/Kg/day)
C57BL/6
CCl4
F
Oil IgG
CCl4 IgG
CCl4 IgG HCQ
Oil α-DBI
CCl4 α-DBI
CCl4 α-DBI HCQ
G
Liver fibrosis score
0.0002
0.0034
0.0408
H
ALT Activity (U/L)
0.0004
0.0094
0.0213
Oil IgG
Oil α-DBI
CCl4 IgG
CCl4 α-DBI
CCl4 α-DBI HCQ
CCl4 IgG HCQ
I
Group
Col1a1
Acat2
Des
Vim
Pdgfa
Pdgfb
Pdgfra
Pdgfrb
pro-fibrotic markers
Tnfa
Il6
Nlrp3
Il1b
pro-inflammatory markers
F4/80
Cd68
Mcp1
macrophage markers
Cat
Gpx1
Sod2
Sod1
Nrf2
Gsr
Hmox1
anti-oxidative stress markers
Group
Oil IgG
Oil α-DBI
CCl4 IgG
CCl4 α-DBI
CCl4 α-DBI HCQ
CCl4 IgG HCQ
Comparison
Oil IgG vs Oil α-DBI
Oil IgG vs CCl4 IgG
CCl4 IgG vs CCl4 α-DBI
CCl4 α-DBI vs CCl4 α-DBI HCQ
CCl4 IgG vs CCl4 IgG HCQ
log2(value)
p_value
0.00
0.05
0.06
1.00

Figure 6

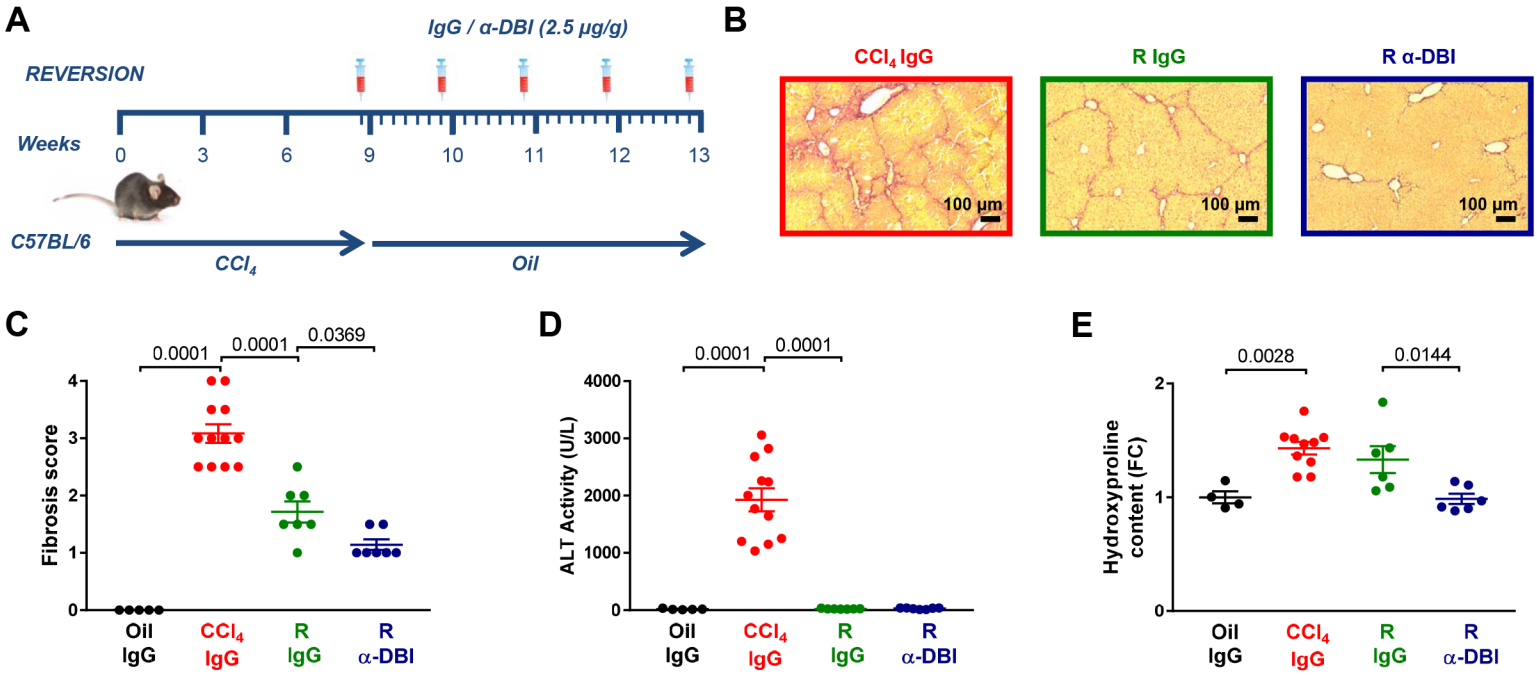
A
IgG / α-DBI (2.5 μg/g)
REVERSION
Weeks
0
3
6
9
10
11
12
13
C57BL/6
CCl4
Oil
B
CCl4 IgG
R IgG
R α-DBI
100 μm
100 μm
100 μm
C
Fibrosis score
0.0001
0.0001
0.0369
Oil IgG
CCl4 IgG
R IgG
R α-DBI
D
ALT Activity (U/L)
0.0001
0.0001
Oil IgG
CCl4 IgG
R IgG
R α-DBI
E
Hydroxyproline content (FC)
0.0028
0.0144
Oil IgG
CCl4 IgG
R IgG
R α-DBI

Figure 7

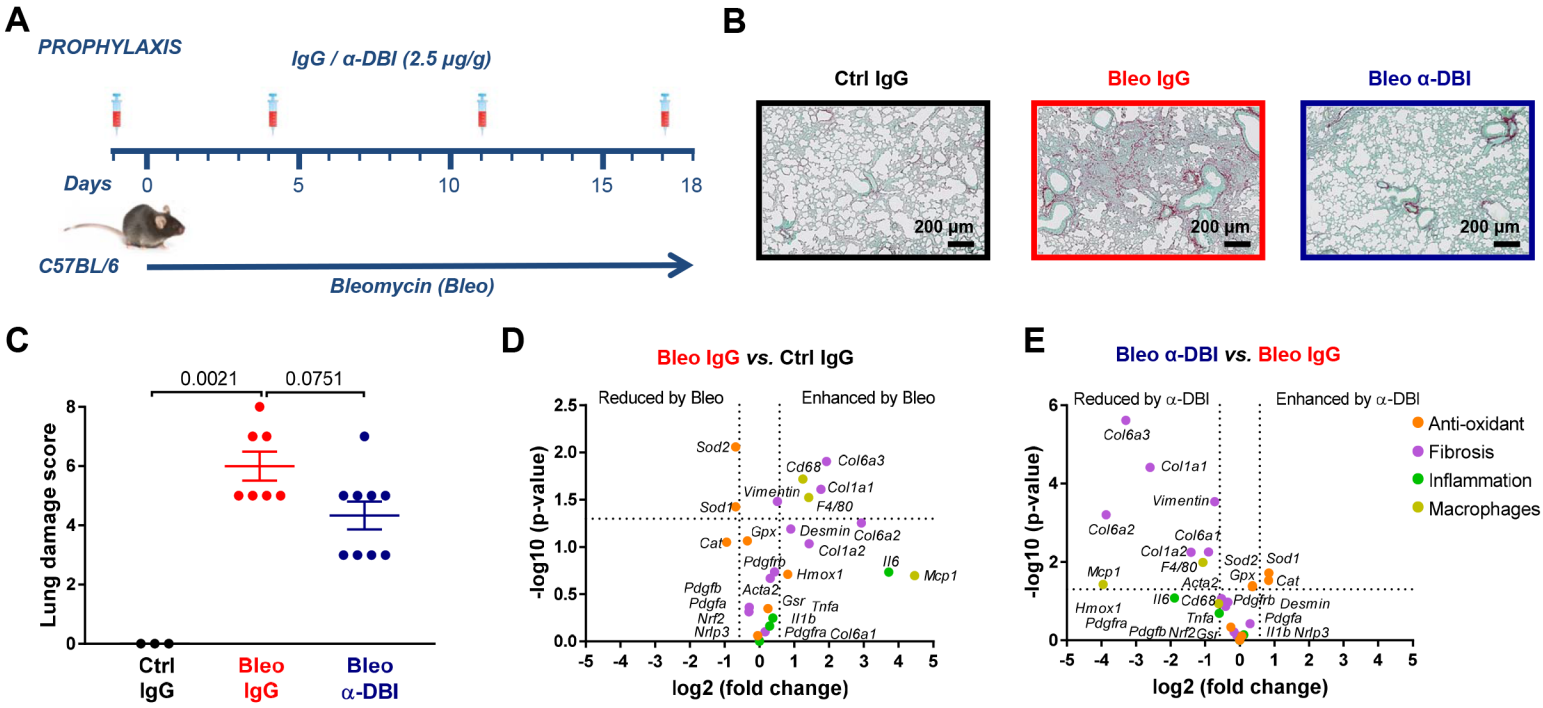
A
PROPHYLAXIS
IgG / α-DBI (2.5 μg/g)
Days
0
5
10
15
18
C57BL/6
Bleomycin (Bleo)
B
Ctrl IgG
Bleo IgG
Bleo α-DBI
200 μm
200 μm
200 μm
C
0.0021
0.0751
Lung damage score
Ctrl IgG
Bleo IgG
Bleo α-DBI
D
Bleo IgG vs. Ctrl IgG
Reduced by Bleo
Enhanced by Bleo
-log10 (p-value)
log2 (fold change)
Sod2
Cd68
Col6a3
Vimentin
Col1a1
Sod1
F4/80
Cat
Gpx
Desmin
Col6a2
Col1a2
Pdgfrb
Hmox1
Il6
Mcp1
Pdgfb
Acta2
Pdgfa
Gsr
Tnfa
Nrf2
Il1b
Nrlp3
Pdgfra
Col6a1
E
Bleo α-DBI vs. Bleo IgG
Reduced by α-DBI
Enhanced by α-DBI
-log10 (p-value)
log2 (fold change)
Anti-oxidant
Fibrosis
Inflammation
Macrophages
Col6a3
Col1a1
Vimentin
Col6a2
Col6a1
Col1a2
F4/80
Sod2
Sod1
Mcp1
Gpx
Cat
Acta2
Il6
Cd68
Pdgfrb
Desmin
Hmox1
Tnfa
Pdgfa
Pdgfra
Pdgfb
Nrf2
Gsr
Il1b
Nrlp3

Figure 8

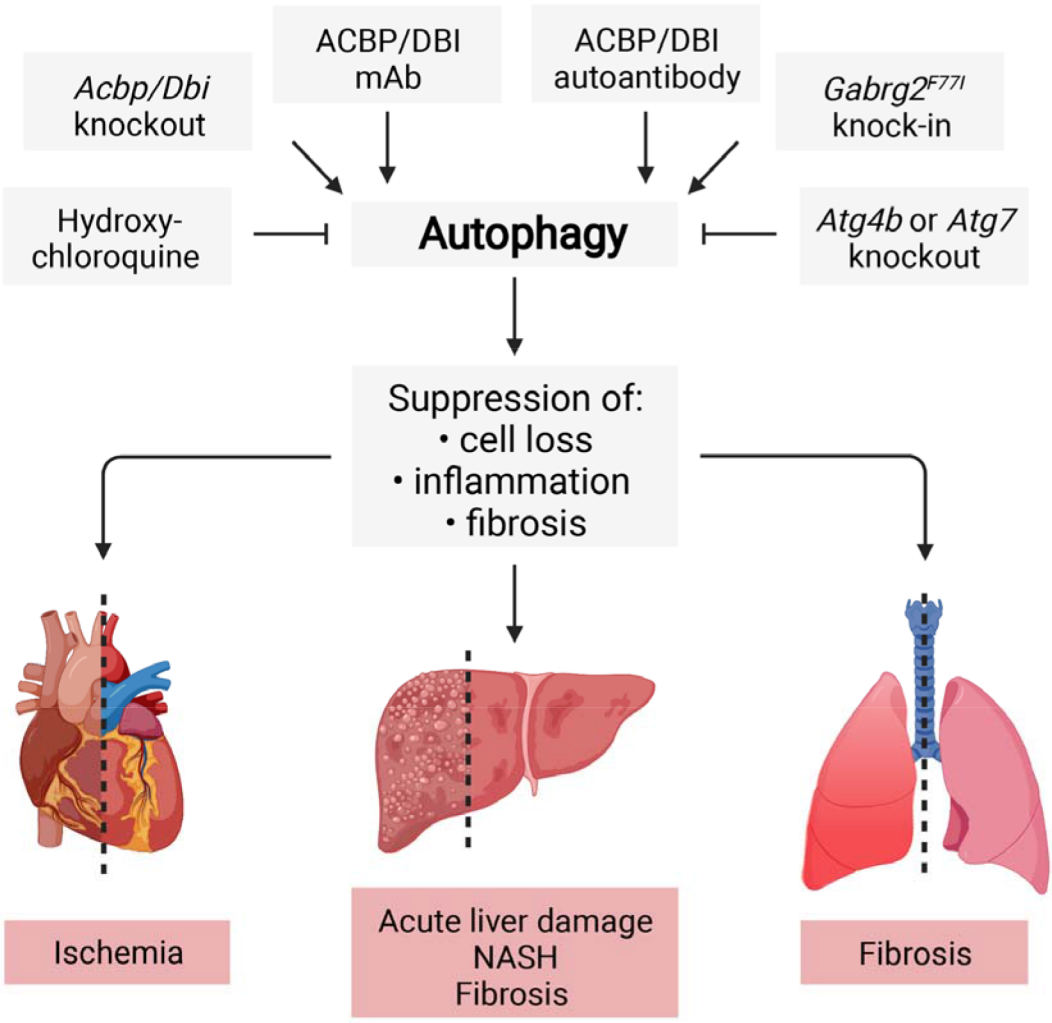
Acbp/Dbi knockout
ACBP/DBI mAb
ACBP/DBI autoantibody
Gabrg2F77I knock-in
Hydroxy-chloroquine
Autophagy
Atg4b or Atg7 knockout
Suppression of:
• cell loss
• inflammation
• fibrosis
Ischemia
Acute liver damage
NASH
Fibrosis
Fibrosis

Figure 9

PNAS

Main Manuscript for

ACBP/DBI protein neutralization confers autophagy-dependent organ protection through inhibition of cell loss, inflammation and fibrosis

Omar Motiño[1-2], Flavia Lambertucci[1-2*], Gerasimos Anagnostopoulos[1-3*], Sijing Li[1-3*], Jihoon Nah[4], Francesca Castoldi[5], Laura Senovilla[1-2,6], Léa Montégut[1-3], Hui Chen[1-2], Sylvère Durand[1-2], Mélanie Bourgin[1-2], Fanny Aprahamian[1-2], Nitharsshini Nirmalathasan[1-2], Karla Alvarez-Valadez[1-3], Allan Sauvat[1-2], Vincent Carbonnier[1], Mojgan Djavaheri-Mergny[1-2], Federico Pietrocola[5], Junichi Sadoshima[4], Maria Chiara Maiuri[1-2], Isabelle Martins[1-2#], and Guido Kroemer[1-2, 7-8#]

[1] Centre de Recherche des Cordeliers, Equipe labellisée par la Ligue contre le cancer, Université de Paris, Sorbonne Université, Inserm U1138, Institut Universitaire de France, Paris, France.

[2] Metabolomics and Cell Biology Platforms, Institut Gustave Roussy, Villejuif, France.

[3] Faculté de Médecine, Université de Paris Saclay, Kremlin Bicêtre, France.

[4] Department of Cell Biology & Molecular Medicine, New Jersey Medical School- Rutgers, The State University of New Jersey, Newark, NJ, USA.

[5] Department of Bioscience and Nutrition, Karolinska Institute, Huddinge, Sweden.

[6] Unidad de Excelencia Instituto de Biología y Genética Molecular (IBGM), Universidad de Valladolid - CSIC, Valladolid, Spain.

[7] Pôle de Biologie, Hôpital Européen Georges Pompidou, AP-HP, Paris, France.

[8] Lead contact.

[#]Correspondence: Guido Kroemer (Kroemer@orange.fr) or Isabelle Martins (isabelle.martins@inserm.fr).

[*]These authors contributed equally to this work.

Supplemental information

Material and Methods

Chemicals and reagents

Reagents were obtained from Axon Medchem BV (Groningen, Netherlands), Qiagen (Hilden, Germany), Millipore (MA, USA), Randox (Antrim, UK), Roche Applied Science (Upper Bavaria, Germany) and Sigma Aldrich (MO, USA). Reagents for electrophoresis were obtained from Thermo Fisher Scientific (MA, USA) and BioRad (CA, USA). Antibodies were from Abcam (TX, USA), Abnova (Taipei, Taiwan), Cell Signaling (MA, USA) and Sigma Aldrich.

Biochemical assays

Plasma ALT and AST activity was determined by colorimetric kits (Randox) accordingly with the manufacturer's instructions. The levels of cytokine were measured by Luminex analysis (Luminex FlexMap 3D). To quantify collagen, hepatic hydroxyproline content was assayed by means of a commercial kit (Sigma Aldrich).

Animal experimentation

Wild-type (*Wt*) C57BL/6 mice (Envigo, Gannat, France), homozygous *Atg4b*$^{-/-}$ mice (gift of Dr. Carlos Lopez-Otin, University of Oviedo, Spain), tamoxifen-inducible whole-body knockout of *floxed Acbp/Dbi*$^{-/-}$ mice (*UBC-cre/ERT2*::*Acbp/Dbi*$^{fl/fl}$, control: Acbp/Dbi$^{fl/fl}$ without CRE) (1), homozygous *Gabrg2* $^{mut/mut}$ mice (bearing a point mutation F77I in the binding site of ACBP/DBI in the gamma-aminobutyric acid A Receptor γ2 subunit) (2), and transgenic mice expressing LC3 conjugated to green fluorescent protein (GFP-LC3-Tg) (3) were bred and maintained according to the FELASA guidelines and local guidelines from the Animal Experimental Ethics Committee (Permissions #25000, #31411, #34537, #34538, and #34539). Homozygous *Atg7*$^{-/-}$ (*Atg7*$^{fl/fl}$*, αMHC Cre*+, control: *Atg7*$^{fl/fl}$*, αMHC Cre*-) and Mito-Keima transgenic mice (4) were used according to the National Institutes of Health guide for the care and use of laboratory animals (NIH Publications No. 8023, revised 1978). Mice were housed in a temperature-controlled environment with 12 h light/dark cycles and were fed with diet and water ad libitum. All animals were sacrificed, and the heart, liver and lung were snap-frozen in liquid nitrogen and stored at -80°C, or fixed in 4% buffered paraformaldehyde overnight at 4°C and embedded in paraffin. Plasma was obtained by cardiac punction.

Neutralization of DBI by passive or active immunization

The monoclonal antibody against DBI (passive immunization) or isotype IgG (Bioxcell, NH, USA) was used in vivo (2.5 µg/g body weight, B.W., intraperitoneally, i.p., in 200 µL) in a single or several

doses. In some experiment, leupeptin (Leu, 30 mg/kg B.W.) was injected i.p. injection 2 h before the end of the experiment.

The production of autoantibodies (active immunization) was induced by conjugation of Keyhole limpet hemocyanin (KLH; from Thermo) and mouse recACBP (KLH-DBI) as Montégut *et al.* described (5). Briefly, KLH and DBI were mixed at a 1:20 molar ratio and adjusted gradually to 0.25% (v/v) glutaraldehyde. After, the glycine solution was added to finish the reaction, and was ultra-filtrated using a 100 KDa membrane (Millipore). A solution of formaldehyde was added to 0.2% (v/v) final concentration, and the reaction was quenched by addition of a glycine solution followed by an ultrafiltration with 70 mM pH 7.8 phosphate buffer. Male 8-week-old C57BL/6 mice were immunized with i.p. injection of 30, 30, 30, 10 µg of KLH-DBI or KLH alone as an adjuvant emulsion (1:1) with Montanide ISA-51vg (Seppic, Paris, France) on days 0, 7, 14 and 21, respectively.

Cardiac injury *in vivo*

Male three-month-old *Wt* and *Atg7*$^{-/-}$ mice were anesthetized by i.p. injection of 60 µg/g pentobarbital sodium and subjected to 3 hours of ischemia by permanent left anterior descending coronary artery (LAD) ligation (6) After sacrifice, hearts were harvested and subjected to 1% Alcian Blue and 1% TTC (2,3,5-triphenyltetrazolium chloride) staining by perfusion (7).

Acute liver damage in mice

To induce hepatic ischemia reperfusion injury, male 12-week-old C57BL/6 mice were anesthetized with 2% isoflurane, and a model of segmental (70%) warm hepatic I/R protocol was assessed (8). Briefly, liver ischemia was induced for 90 min, and reperfusion was initiated by removal of the clamp for 4 hours. To induce hepatotoxicity, male 12-week-old C57BL/6 mice were treated with 12 mg/kg Concanavalin A (ConA, Sigma Aldrich) or 300 mg/kg acetaminophen (APAP, Sigma Aldrich) for 4 or 16 hours, respectively. For inhibition of the autophagy flux, the animals were injected i.p. with two doses of 50 mg/kg hydroxychloroquine (HCQ, in PBS; Axon Medchem BV) 4 hours and just before the hepatic damage**.**

NASH and hepatic fibrosis model *in vivo*

Male 2-3 months old mice were fed with regular chow diet (RCD) or methionine choline-deficient diet (MCD; AIN-76 Safe diet, Essingen, Germany) for 4 weeks as preventive model (prophylaxis). Some mice were fed with MCD diet for 4 weeks and then with RCD diet for another 4 days as a diet recovery model (reversion, R). For inhibition of β-oxidation, etomoxir (ETO, Sigma Aldrich) was injected i.p. 2 hours after R and then daily into C57BL/6 mice. To induce fibrosis in the liver, CCl_4 (Sigma Aldrich) was i.p. administered to male 2-months-old C57BL/6 mice at a dose of 1.6 ml/kg

twice weekly for 9 weeks (9). Control animals were i.p. injected with the vehicle olive oil (Sigma Aldrich). Additional groups were administrated i.p. with 50 mg/kg HCQ daily for the four last weeks of CCl_4. Another approach to induce hepatic fibrosis involved by bile duct ligation (BDL) for 2 weeks (10).

Pulmonary fibrosis in mice

To induce lung fibrosis, male 2-3 months old was administrated intratracheally with one single dose of 2 mg/kg bleomycin and the animals were sacrificed after 18 days (11).

Histopathology

Paraffin-embedded sections (5 µm) were stained with hematoxylin-eosin-safranin (HES) or Sirius Red and were evaluated by experienced pathologist blinded to the features of the animal groups. All slides were scanned with an AxioScan Z1 (Carl Zeiss, Jena, Germany). The NAFLD activity score was assessed using the NAFLD scoring system for mice models validated by Liang *et al.* (12). Briefly, steatosis grade was grouped as follows: grade 0, <5% of steatotic hepatocytes; grade 1, 5–33%; grade 2, 33–66%; and grade 3, >66%. Lobular inflammation was scored as follows: 0, no foci; 1, <2 foci; 2, 2–4 foci; and 3, >4 foci. Ballooning was classified as 0, none; 1, few balloon cells; and 2, many balloon cells. NAFLD activity score was calculated for each liver biopsy based on the sum of scores for steatosis, inflammation, and ballooning. In addition, liver fibrosis staging (Metavir score) was defined as 0, none; 1, perisinusoidal and/or pericentral; 2, incomplete central/central bridging fibrosis; 3, complete central/central bridging fibrosis; and 4, definite cirrhosis (13). The severity of hepatic IR was graded according to Suzuki's criteria on a scale from 0 to 4. None (0%), minimal (10%), mild (11-30%), moderate (30-60 %) and severe (>60%) necrosis, congestion, or centro-lobular ballooning was assigned as grade 0, 1, 2, 3 and 4, respectively (14). To measure APAP hepatotoxicity, liver samples were classified as none (0; 0%), mild (1; less than 20%), moderate (2; 20 ~ 70%,), severe (3; more than 70% of hepatic lobules), taking account of the cell death area, ballooning, and inflammation around the central veins (15). The hepatic injury induced by ConA was scored using grades as follows: 0, no necrotic infiltrates; 1, small foci of necrotic cells between hepatocytes or necrotic cells surrounding individual hepatocytes; 2, larger foci of 100 necrotic cells or involving 30 hepatocytes; 3, 10% of a hepatic cross-section involved; and 4, 30% of a hepatic cross-section involved (Zhao et al., 2020). The pulmonary damage/fibrosis was assessed by the Ashcroft score: 0, normal lung; 1, minimal fibrosis thickening of wall without obvious damage to lung architecture; 3, moderate fibrosis thickening of wall without obvious damage to lung architecture; 5, increased fibrosis with definite damage to lung structure and formation of fibrous bands or fibrous small masses; 7, severe distortion of structure and large fibrosis areas ("Honeycumb lung" is placed in this category); and 8, total fibrous obliteration of the

field (17). Also, to determinate the abundance of hepatic macrophages and Kupffer cells, liver sections from fixed paraffin blocks were immunohistochemically stained according to standard procedures using anti-mouse F4/80.

Liver extracts

For protein or RNA extraction, tissues were homogenized in 2 cycles for 20 s at 5,500 rpm using a Precellys 24 tissue homogenator (Bertin Technologies, Montigny-le-Bretonneux, France) in 20 mM Tris buffer (pH 7.4) containing 150 mM NaCl, 1% Triton X-100, 10 mM EDTA and Complete® protease inhibitor cocktail (Roche Applied Science) or QIAzol (Qiagen), respectively. After, protein extracts were centrifuged at 12,000 g (4 ºC) for 15 min and supernatants were collected. Protein concentration in supernatants was evaluated by the bicinchoninic acid technique (BCA protein assay kit, Thermo Fisher Scientific). Homogenate RNA was purified with RNeasy Mini Kit (Qiagen) following the manufacturer's instructions. The purify and concentration of RNA was measured by NanoDrop™ (Thermo Fisher Scientific).

Whole transcriptome analysis

For RNA-sequencing library preparation, RNA was extracted from mouse livers using RNA Plus Mini Kit (Qiagen) according to manufacturer's instructions. The concentration and integrity of total RNA was analyzed using electrophoretic separation on microfabricated chips in Agilent 2100 Bioanalyzer System (Agilent, CA, USA). After, mRNA-sequencing library preparation (1.5 µg total RNA per sample) was carried out on NovaSeq 6000 PE150 instrument (2 x 150 bp, 40 million reads per sample). For RNA-sequencing data analysis, pseudo-alignment and quantification were carried-out with HISAT2 algorithm (reference genome GRCm39) (18). Then, the correlation analysis of the principal component study and differential expression analysis were performed with DESeq2 package (19). To study the differential gene expression, the analyses were ran using the parametric Wald test with Benjamini-Hochberg adjustment (*p*-adj). Genes were expressed using Z-Score normalization and were considered significantly differentially expressed when p-adj <0.05 and $\log^2$ (fold change) (cut-off) was ≥±1.5. GSEA (Gene Set Enrichment Analysis), based gene ontology (GO) and Kyoto Encyclopedia of Genes and Genomes (KEGG) analyses were performed on RNA-seq data from liver samples (20). A web-based bioinformatics tool (http://www.bioinformatics.com.cn) was used to draw the graph.

Analysis of GEO datasets

The genes over-expressed in human liver samples from NAFLD/NASH compared with normal livers in ten Gene Expression Omnibus (GEO) datasets (GSE159676, GSE151158, GSE63067, GSE48452, GSE17470, GSE66676, GSE24807, GSE33814, GSE126848, and GSE135251) were

identified by the GEO2R tool or the stats package in R software (version 4.1.0). The genes reduced by α-DBI in MCD experiments were detected by the stats package in R software. The overlap of genes between datasets, α-DBI down-regulates genes that are upregulated in human NAFLD/NASH, were selected by means of a Venn diagram. The overlap representation factor (ORF) is the ratio between actual overlap on theoretical overlap, which is calculated by the formula ORF=x * N / (n1 * n2), with x=number of genes in common between two groups, N=total unique genes of two groups, n1=number of genes in group 1, n2=number of genes in group 2. The *p* value was calculated by means Fisher's exact test.

Gene expression analyses

Total RNA (1 µg) was reverse transcribed using the SuperScript™ VILO™ cDNA Synthesis Kit (Invitrogen). Quantitative real-time PCR was performed with a StepOnePlus Real-Time PCR System (Applied Biosystems, Thermo Fisher Scientific) sequence detector using the Master Mix PCR Power SYBR™ Green (Applied Biosystems, Thermo Fisher Scientific) and d(N)6 random hexamer with the primers described in the Table S2. Specific primers were purchased from Sigma. PCR thermocycling parameters were 95 °C for 1min, 40 cycles of 95 °C for 15 s, and 60 °C for 1 min. Each sample was run in duplicate and was normalized to 36b4 mRNA expression levels. Then, the replicates were averaged, and fold induction was determined as ΔΔCt based fold-change.

Western Blots

For immunoblotting, whole-cell extracts were boiled for 5 min in Laemmli sample buffer, and equal amounts of protein (20–30 µg) were separated on 4-12% Bis-Tris acrylamide precast gels (Thermo Fisher Scientific) and electro-transferred to PDVF membranes (BioRad). Membranes were horizontally sliced according to the molecular weight of the protein of interest to allow simultaneous detection within the same experiment. Unspecific binding sites were saturated by incubating membranes for 1 h in 0.05% Tween 20 (v:v in TBS) supplemented with 5% non-fat powdered milk (w:v in TBS). The relative amount of each protein was determined by overnight incubation with primary antibodies specific for ACBP/DBI, α-SMA, ATG4B, CATALASE, CPT1A, COLLAGEN 1A1, HMOX1, MAP1LC3B/LC3B, PPAR-α, SOD2, and SQSTM1/p62 (Table S2). Glyceraldehyde-3-phosphate dehydrogenase antibody (Table S2) was used to control equal loading of lanes. The blots were revealed with appropriate horseradish peroxidase (HRP)-labeled secondary antibodies (Southern Biotech, AL, USA) plus SuperSignal West Pico chemoluminescent substrate (Thermo Fisher Scientific) and different exposition times were performed for each blot with a charged coupling device camera in a luminescent image analyzer LAS 4000 (GE Healthcare, IL, USA) to ensure the linearity of the band intensities. Densitometric analysis of the bands was carried out using ImageJ software (http://imagej.nih.gov) and expressed in relative expression.

Quantitative analysis of autophagy biosensors in tissues

Hearts from Mito-Kemia transgenic mice and liver from LC3-GFP transgenic mice were collected and fixed with 4% paraformaldehyde (in PBS, pH 7.4) for at least 16 h, followed by treatment with 30% sucrose (in PBS) overnight at 4°C. Samples were embedded in Tissue-Tek OCT compound (Sakura Finetechnical, Tokyo, Japan) and stored at -80 °C. Five µm-thick tissue sections were prepared with a Cryostat CM3050S S cryostat (Leica Microsystems), air-dried for at least 1 hour, washed in PBS for 5 min, dried at RT for 30 min, and mounted with DAPI Fluoromount-G® anti-fading medium (SouthernBiotech, AL, USA) . Then, the slides were scanned using a LSM 710 confocal fluorescence microscope (Carl Zeiss, Jena, Germany). Livers or hearts from mice expressing GFP-LC3 were subjected to a similar histological analysis. GFP-LC3 dots were quantified in three independent visual fields from at least three mice per group, using Image J software.

Metabolomics liver sample preparation

First, 30 mg of livers were weighted and transferred to 2 mL-homogenizer tube with ceramic beads (Hard Tissue Homogenizing CK28, 2.8 mm zirconium oxide beads; Precellys, Bertin Technologies), containing 1 mL of ice-cold extraction mixture (metOH/water, 9/1, -20°C, with a cocktail of internal standards). To facilitate solvent access and endogenous metabolites extraction, samples were completely homogenized in Precellys 24 tissue homogenize (3 cycles of 20 s/ 5000 rpm). After centrifugation (10 min at 15000 g, 4°C), supernatants were collected. For plasma, samples (25 µL) were mixed with 250 µL of the of ice-cold extraction mixture, allowing protein precipitation and metabolites extraction, then vortexed and centrifuged (10 min at 15000 g, 4°C). Next, tissues or plasma centrifugation, supernatants were collected, split in 3 fractions, and treated following published protocols (21). Briefly, they extract were split in 3 fractions: first fraction for short chain fatty acids analysis (40 µL for both tissues and plasma samples) were derivatized before injection, 2nd fraction for LC/MS and 3d fraction for GC/MS analyses (300 µL/each for tissue and 100 µL/each for plasma samples) were transferred to an injection amber glass vial (with fused-in insert) and evaporated to dryness (Techne DB3, Staffordshire, UK) at 40°C. The second dried fraction was recovered with 200 µL or 150 µL (tissue or plasma samples, respectively) of ultra-pure water and kept at -80°C until injection and analysis by LC/MS. The third dried fraction was derivatized before GC/MS injection and analysis. Finally, the 4th fraction together with the sample pellet were re-extracted with an equal volume of 2% SSA (in methanol), vortexed and centrifuged (10 min at 15000 g, 4°C). The supernatant (350 and 60 µL, from tissue and plasma extracts, respectively) was transferred to an injection polypropylene vial (with fused-in insert) and evaporated to dryness (Techne DB3, Staffordshire, UK) at 40°C. Dried samples were dissolved with ultra-pure water (200

and 100 µL, for tissue and plasma dried extracts, respectively) and kept at -80°C until injection and analysis by UHPLC/MS for polyamines detection.

Metabolomic analysis

Targeted analysis of nucleoside phosphates and cofactors by ion pairing Ultra-High Performance Liquid Chromatography (UHPLC) coupled to a Triple Quadrupole (QQQ) mass spectrometer: Targeted UHPLC/MS analyses were performed on a UHPLC 1290 system (Agilent), with an autosampler kept at 4°C, and a pellet oven for rigorous control of the column temperature. The UHPLC was coupled to a QQQ/MS 6470 (Agilent) equipped with an electrospray source, using nitrogen as collision gas. Short chain fatty acids and ketones bodies were detected in the 1st fraction after injection of 10 µL of sample were into a Zorbax Eclipse XDB-C18 (100 mm x 2.1 mm, particle size 1.8 µm; Agilent) column protected by a guard column C18 (5 mm × 2.1 mm, particle size 1.8 µm). Column oven maintained at 50°C during analysis. The gradient mobile phase consisted of 0.01 % formic acid (Sigma Aldrich) (A) and ACN (0.01 % formic acid) (B). The flow rate was set to 0.7 ml/min, and gradient as follow: 20% B (initial conditions) maintained for 3 min, to 45% B in 4 min; then 95% B maintained 2 min, and finally equilibration to initial conditions, 20% B, for 1 min. The QQQ/MS was operated in negative mode. The gas temperature was set to 300°C with a gas flow of 12 L/min. The capillary voltage was set to 5 kV.

For bile acid detection, 5 µL from samples recovered in water (2nd fraction), were injected into a Poroshell 120 EC-C8 (100 mm x 2.1 mm particle size 2.7 µm; Agilent technologies) column protected by a guard column (XDB-C18, 5 mm × 2.1 mm particle size 1.8 µm). Mobile phase consisted of 0.2% formic acid (A) and ACN/IPA (1/1; v/v) (B) freshly made. Flow rate was set to 0.5 mL/min, and gradient as follow: 30% B increased to 38% B over 2 min; maintained for 2 min then increased 60% for 1.5 minutes, and finally to 98% B for 2 minutes (column washing), followed by 2 min of column equilibration at 30% B (initial conditions). The QQQ/MS was operated in negative mode. Gas temperature and flow were set to 310°C and 12 L/min, respectively. Capillary voltage was set to 5 kV. Polyamines were detected in the 4th fraction after injection of 10 µL of sample were into a Kinetex C18 (150 mm x 2.1 mm particle size 2.6 µm; Phenomenex) column protected by a guard column C18 (5 mm × 2.1 mm, particle size 1.8 µm). Column oven maintained at 40°C during analysis. The gradient mobile phase consisted of 0.1 % HFBA (Sigma) (A) and ACN (0.1 % HFBA) (B) freshly made. The flow rate was set to 0.4 ml/min, and gradient as follow: from 5% (initial conditions) to 30% B in 7 min; then 90% B maintained 2 min, and finally equilibration to initial conditions, 5% B, for 2 min. The QQQ/MS was operated in positive mode. The gas temperature was set to 350°C with a gas flow of 12 L/min. The capillary voltage was set to 2.5 kV. In addition, tissue samples were injected for the analysis of nucleotides and co-factors into a Zorbax Eclipse plus C18 (100 mm × 2.1 mm, particle size 1.8 µm, Agilent) column protected by a guard column

C18 (5 mm × 2.1 mm, particle size 1.8 µm). Column oven maintained at 40°C during analysis. The gradient mobile phase consisted of 0.5 mM DBAA (Sigma) (A) and ACN (B). The flow rate was set to 0.4 mL/min, and gradient as follow: 10% B (initial conditions) maintained for 3 min, then increased to 95% B in 1 min and maintained 2 min, to finally equilibrate to initial conditions, 10% B, for 1 min. The QQQ/MS was operated in both positive and negative mode. The gas temperature was set to 350°C with a gas flow of 12 L/min. The capillary voltage was set to 4.5 kV in positive mode and 5 kV in negative mode. MRM scan mode was used for targeted analysis in both GC and UHPLC/MS. Peak detection and integration were performed using the Agilent Mass Hunter quantitative software (B.10.1).

Widely targeted analysis of intracellular metabolites. GC/MS: Derivatized samples for GC/MS analysis (3d fraction) were injected (1 µL) into a gas chromatograph (Agilent 7890B; Agilent Technologies, Waldbronn, Germany) coupled to a triple quadrupole mass spectrometer (QQQ/MS; 7000C Agilent Technologies, Waldbronn, Germany), equipped with a high sensitivity electronic impact source (EI) operating in positive mode. Injection was performed in splitless mode. Front inlet temperature was kept at 250°C, transfer line and ion-source temperature were 250°C and 230°C, respectively. Septum purge flow was fixed at 3 mL/min, purge flow to split vent operated at 80 mL/min during 1 min and gas saver mode was set to 15 mL/min after 5 min. Helium gas flowed through column (HP-5MS, 30m x 0.25 mm, i.d. 0.25 mm, d.f. J&WScientific, Agilent Technologies Inc.) at 1 mL/min. Column temperature was held at 60°C for 1 min, raised to 210°C (10°C/min), then to 230°C (5°C/ min), to finally reach 325°C (15°C/min). The collision gas was nitrogen.

Pseudo-targeted analysis of intracellular metabolites. **UHPLC/MS:** The profiling analysis was performed with a Dionex Ultimate 3000 UHPLC system (Thermo Fisher Scientific) coupled to an Orbitrap mass spectrometer (q-Exactive, Thermo Fisher Scientific) equipped with an electrospray source operating in both positive and negative mode, and acquired samples in full scan analysis mode, from 100 to 1200 m/z. LC separation was performed on reversed phase (Zorbax Sb-Aq 100 x 2.1 mm x 1.8 µm particle size), with mobile phases: 0.2% acetic acid (A), and ACN (B). Column oven was kept at 40°C. Ten microliters of aqueous sample (2^{nd} fraction) were injected for metabolite separation with a gradient starting from 2% B, increased to 95% B in 22 min, and maintained during 2 min for column rinsing, followed by column equilibration at 2% B for 4 min. Flow rate was set to 0.3 mL/min. The q-Exactive parameters were: sheath gas flow rate 55 au, auxiliary gas flow rate 15 au, spray voltage 3.3 kV, capillary temperature 300°C, S-Lens RF level 55 V. The mass spectrometer was calibrated with sodium acetate solution dedicated to low mass calibration. Data were analyzed with the quantitative node of Thermo Xcalibur (version 2.2) in a pseudo-targeted approach with a home-based metabolites list.

Proposal model

The proposal model was created with BioRender.com with number of agreement BK246PS4V0.

Data analysis

Data are expressed as means ± SEM. For statistical analysis, firstly, the normal distribution of the results was evaluated by D'Agostino & Pearson normality test, Shapiro-Wilk normality, and Kolmogorov-Smirnov test. For Gaussian distributions, unpaired two-tailed Student´s t-test or one-way analysis of variance (ANOVA) followed by Sidak post hoc multiple comparison test was used for two or multiple comparisons, respectively. For non-Gaussian distributions, the following tests were performed: Mann–Whitney U test was used for two groups and Kruskal–Wallis followed by Dunn post hoc test for multiple groups. Analysis was performed by using the statistical software GraphPad Prism 7. Whole transcriptome sequencing and GEO datasets statistical analysis was tested by Fisher's exact test. For statistical analysis of metabolomic, the *p* value was calculated by Mann-Whitney test. All targeted treated data were merged and cleaned with a dedicated R (version 3.4) package (@Github/Kroemerlab/GRMeta). A $p<0.05$ was considered as statistically significant.

References

1. J. M. Bravo-San Pedro, *et al.*, Acyl-CoA-Binding Protein Is a Lipogenic Factor that Triggers Food Intake and Obesity. *Cell Metab* **30**, 754-767.e9 (2019).

2. P. Wulff, *et al.*, From synapse to behavior: rapid modulation of defined neuronal types with engineered GABAA receptors. *Nat Neurosci* **10**, 923–929 (2007).

3. N. Mizushima, A. Yamamoto, M. Matsui, T. Yoshimori, Y. Ohsumi, In vivo analysis of autophagy in response to nutrient starvation using transgenic mice expressing a fluorescent autophagosome marker. *Mol Biol Cell* **15**, 1101–1111 (2004).

4. M. Tong, *et al.*, Mitophagy Is Essential for Maintaining Cardiac Function During High Fat Diet-Induced Diabetic Cardiomyopathy. *Circ Res* **124**, 1360–1371 (2019).

5. L. Montégut, *et al.*, Immunization of mice with the self-peptide ACBP coupled to keyhole limpet hemocyanin. *STAR Protoc* **3**, 101095 (2022).

6. S. Sciarretta, *et al.*, Trehalose-Induced Activation of Autophagy Improves Cardiac Remodeling After Myocardial Infarction. *J Am Coll Cardiol* **71**, 1999–2010 (2018).

7. S. Venkatesh, *et al.*, Mitochondrial LonP1 protects cardiomyocytes from ischemia/reperfusion injury in vivo. *J Mol Cell Cardiol* **128**, 38–50 (2019).

8. O. Motiño, *et al.*, Protective Role of Hepatocyte Cyclooxygenase-2 Expression Against Liver Ischemia–Reperfusion Injury in Mice. *Hepatology* **70** (2019).

9. O. Motiño, *et al.*, Cyclooxygenase-2 expression in hepatocytes attenuates non-alcoholic steatohepatitis and liver fibrosis in mice. *Biochimica et Biophysica Acta - Molecular Basis of Disease* **1862** (2016).

10. C. G. Tag, *et al.*, Bile Duct Ligation in Mice: Induction of Inflammatory Liver Injury and Fibrosis by Obstructive Cholestasis. *JoVE (Journal of Visualized Experiments)* **96**, e52438 (2015).

11. S. N. Kim, *et al.*, Dose-response Effects of Bleomycin on Inflammation and Pulmonary Fibrosis in Mice. *Toxicological Research* **26**, 217 (2010).

12. W. Liang, *et al.*, Establishment of a general NAFLD scoring system for rodent models and comparison to human liver pathology. *PLoS One* **9** (2014).

13. P. Bedossa, T. Poynard, An algorithm for the grading of activity in chronic hepatitis C. *Hepatology* **24**, 289–293 (1996).

14. S. Suzuki, L. H. Toledo-Pereyra, F. J. Rodriguez, D. Cejalvo, Neutrophil infiltration as an important factor in liver ischemia and reperfusion injury. Modulating effects of FK506 and cyclosporine. *Transplantation* **55**, 1265–1271 (1993).

15. A. Naiki-Ito, *et al.*, Gap junction dysfunction reduces acetaminophen hepatotoxicity with impact on apoptotic signaling and connexin 43 protein induction in rat. *Toxicol Pathol* **38**, 280–286 (2010).

16. J. Zhao, *et al.*, Nicotine attenuates concanavalin A-induced liver injury in mice by regulating the α7-nicotinic acetylcholine receptor in Kupffer cells. *Int Immunopharmacol* **78** (2020).

17. T. Ashcroft, J. M. Simpson, V. Timbrell, Simple method of estimating severity of pulmonary fibrosis on a numerical scale. *Journal of Clinical Pathology* **41**, 467 (1988).

18. D. Kim, J. M. Paggi, C. Park, C. Bennett, S. L. Salzberg, Graph-based genome alignment and genotyping with HISAT2 and HISAT-genotype. *Nat Biotechnol* **37**, 907–915 (2019).

19. M. I. Love, W. Huber, S. Anders, Moderated estimation of fold change and dispersion for RNA-seq data with DESeq2. *Genome Biol* **15** (2014).

20. J. Wang, S. Vasaikar, Z. Shi, M. Greer, B. Zhang, WebGestalt 2017: a more comprehensive, powerful, flexible and interactive gene set enrichment analysis toolkit. *Nucleic Acids Res* **45**, W130–W137 (2017).

21. C. Grajeda-lglesias, *et al.*, Oral administration of Akkermansia muciniphila elevates systemic antiaging and anticancer metabolites. *Aging* **13**, 6375–6405 (2021).

Figure S1

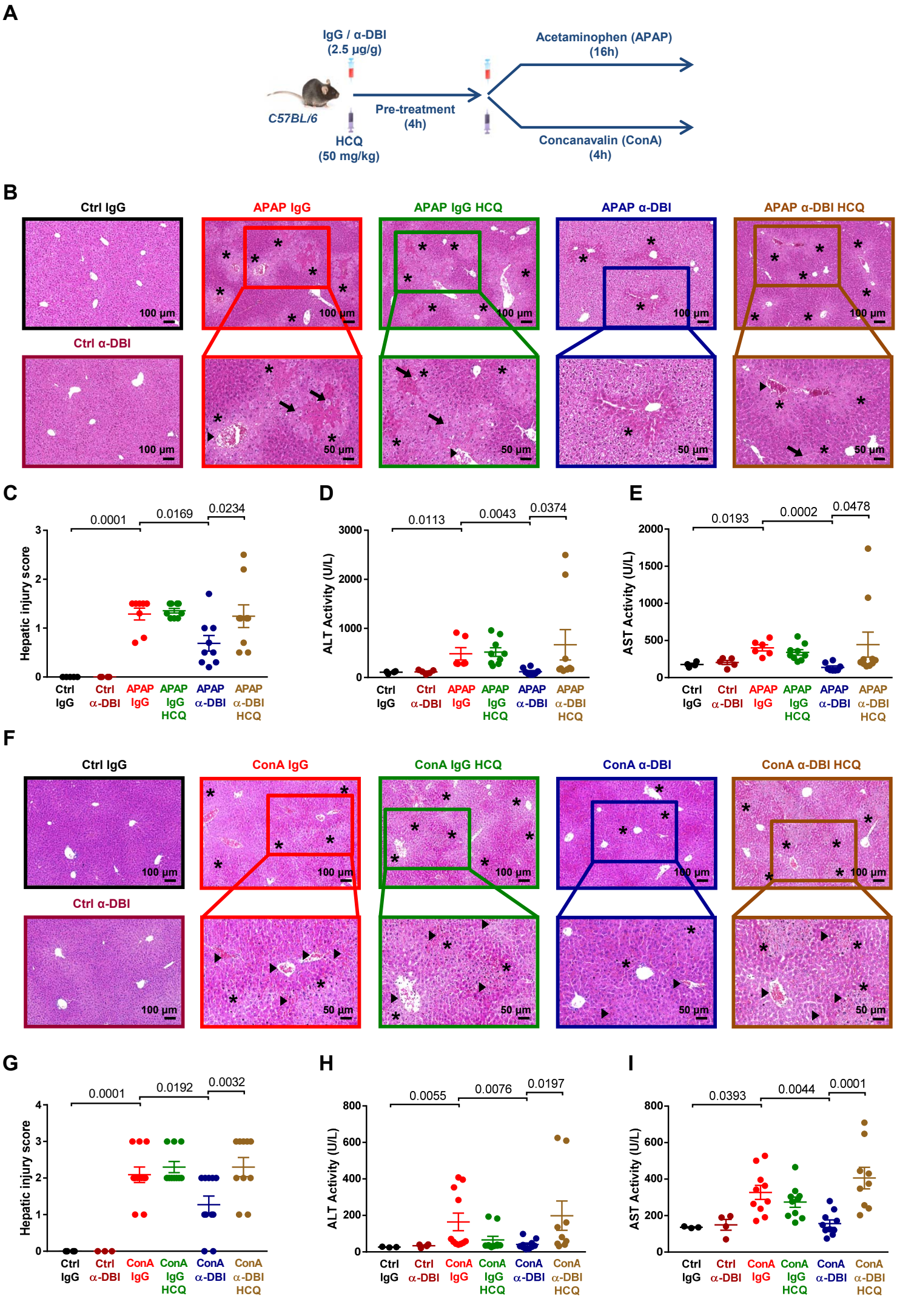
A
IgG / α-DBI
(2.5 μg/g)
C57BL/6
HCQ
(50 mg/kg)
Pre-treatment
(4h)
Acetaminophen (APAP)
(16h)
Concanavalin (ConA)
(4h)
B
Ctrl IgG
APAP IgG
APAP IgG HCQ
APAP α-DBI
APAP α-DBI HCQ
Ctrl α-DBI
100 μm
50 μm
C
Hepatic injury score
0.0001
0.0169
0.0234
D
ALT Activity (U/L)
0.0113
0.0043
0.0374
E
AST Activity (U/L)
0.0193
0.0002
0.0478
Ctrl IgG
Ctrl α-DBI
APAP IgG
APAP IgG HCQ
APAP α-DBI
APAP α-DBI HCQ
F
ConA IgG
ConA IgG HCQ
ConA α-DBI
ConA α-DBI HCQ
G
0.0001
0.0192
0.0032
H
0.0055
0.0076
0.0197
I
0.0393
0.0044
0.0001
ConA IgG
ConA IgG HCQ
ConA α-DBI
ConA α-DBI HCQ

Figure S2

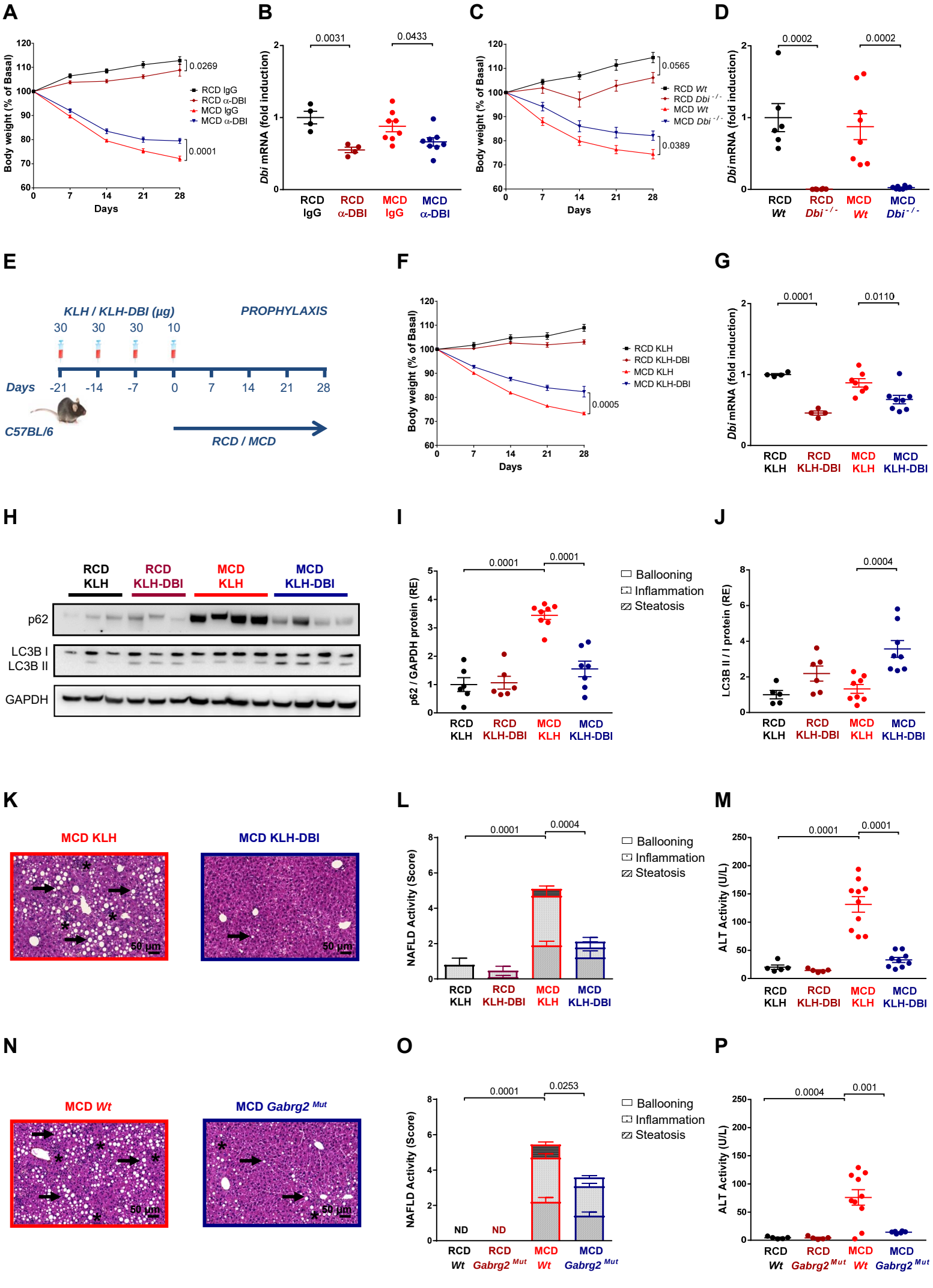
A
Body weight (% of Basal)
Days
RCD IgG
RCD α-DBI
MCD IgG
MCD α-DBI
0.0269
0.0001
B
Dbi mRNA (fold induction)
0.0031
0.0433
RCD IgG
RCD α-DBI
MCD IgG
MCD α-DBI
C
Body weight (% of Basal)
Days
RCD Wt
RCD Dbi -/-
MCD Wt
MCD Dbi -/-
0.0565
0.0389
D
Dbi mRNA (fold induction)
0.0002
0.0002
RCD Wt
RCD Dbi -/-
MCD Wt
MCD Dbi -/-
E
KLH / KLH-DBI (µg)
30
30
30
10
PROPHYLAXIS
Days
-21
-14
-7
0
7
14
21
28
C57BL/6
RCD / MCD
F
Body weight (% of Basal)
Days
RCD KLH
RCD KLH-DBI
MCD KLH
MCD KLH-DBI
0.0005
G
Dbi mRNA (fold induction)
0.0001
0.0110
RCD KLH
RCD KLH-DBI
MCD KLH
MCD KLH-DBI
H
RCD KLH
RCD KLH-DBI
MCD KLH
MCD KLH-DBI
p62
LC3B I
LC3B II
GAPDH
I
p62 / GAPDH protein (RE)
0.0001
0.0001
Ballooning
Inflammation
Steatosis
RCD KLH
RCD KLH-DBI
MCD KLH
MCD KLH-DBI
J
LC3B II / I protein (RE)
0.0004
RCD KLH
RCD KLH-DBI
MCD KLH
MCD KLH-DBI
K
MCD KLH
MCD KLH-DBI
50 µm
50 µm
L
NAFLD Activity (Score)
0.0001
0.0004
Ballooning
Inflammation
Steatosis
RCD KLH
RCD KLH-DBI
MCD KLH
MCD KLH-DBI
M
ALT Activity (U/L)
0.0001
0.0001
RCD KLH
RCD KLH-DBI
MCD KLH
MCD KLH-DBI
N
MCD Wt
MCD Gabrg2 Mut
50 µm
50 µm
O
NAFLD Activity (Score)
0.0001
0.0253
Ballooning
Inflammation
Steatosis
ND
ND
RCD Wt
RCD Gabrg2 Mut
MCD Wt
MCD Gabrg2 Mut
P
ALT Activity (U/L)
0.0004
0.001
RCD Wt
RCD Gabrg2 Mut
MCD Wt
MCD Gabrg2 Mut

Figure S3

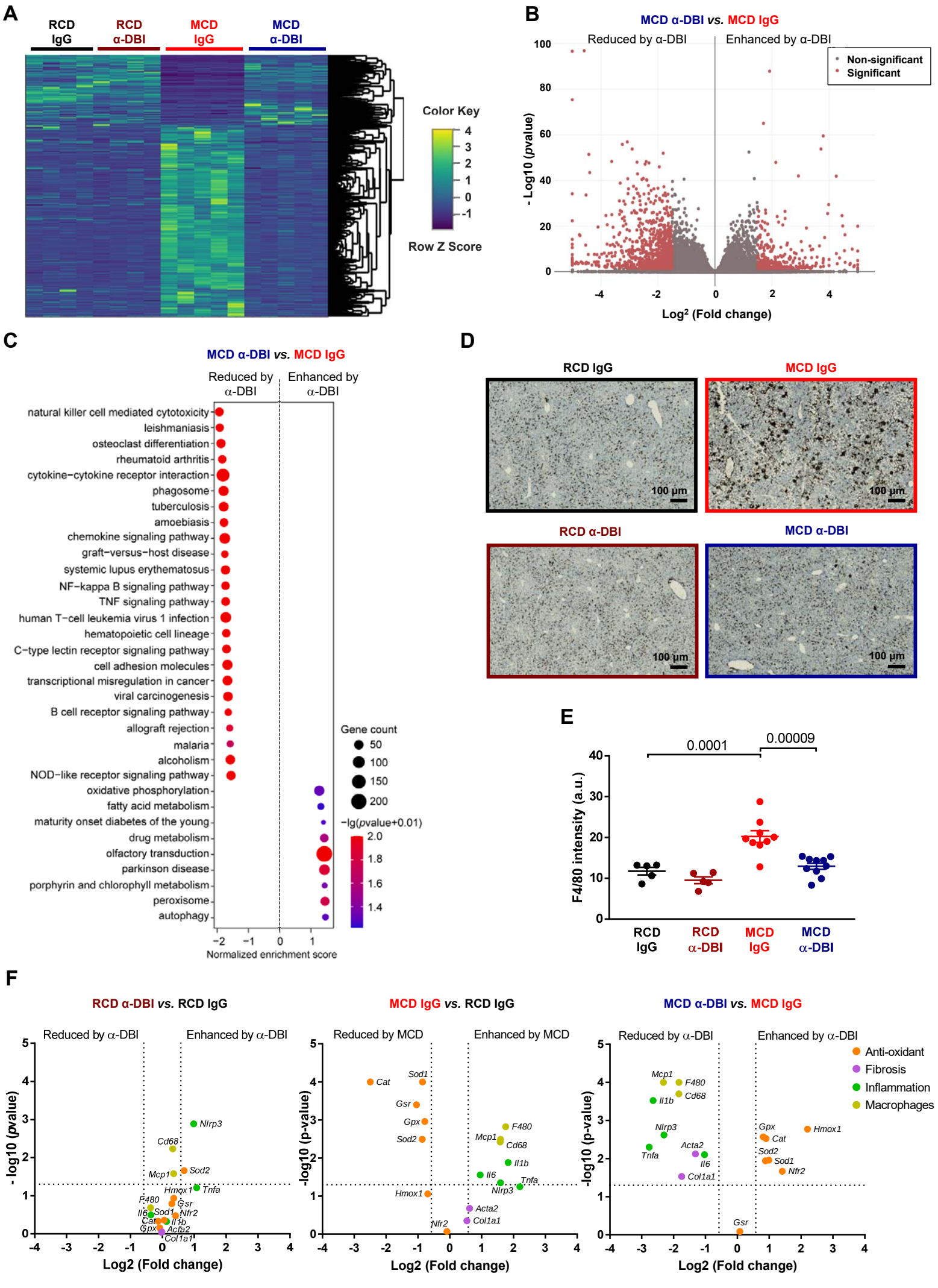
A
RCD IgG
RCD α-DBI
MCD IgG
MCD α-DBI
Color Key
Row Z Score
B
MCD α-DBI vs. MCD IgG
Reduced by α-DBI
Enhanced by α-DBI
Non-significant
Significant
- Log10 (pvalue)
Log² (Fold change)
C
MCD α-DBI vs. MCD IgG
Reduced by α-DBI
Enhanced by α-DBI
natural killer cell mediated cytotoxicity
leishmaniasis
osteoclast differentiation
rheumatoid arthritis
cytokine−cytokine receptor interaction
phagosome
tuberculosis
amoebiasis
chemokine signaling pathway
graft−versus−host disease
systemic lupus erythematosus
NF−kappa B signaling pathway
TNF signaling pathway
human T−cell leukemia virus 1 infection
hematopoietic cell lineage
C−type lectin receptor signaling pathway
cell adhesion molecules
transcriptional misregulation in cancer
viral carcinogenesis
B cell receptor signaling pathway
allograft rejection
malaria
alcoholism
NOD−like receptor signaling pathway
oxidative phosphorylation
fatty acid metabolism
maturity onset diabetes of the young
drug metabolism
olfactory transduction
parkinson disease
porphyrin and chlorophyll metabolism
peroxisome
autophagy
Gene count
−lg(pvalue+0.01)
Normalized enrichment score
D
RCD IgG
MCD IgG
RCD α-DBI
MCD α-DBI
100 μm
E
0.0001
0.00009
F4/80 intensity (a.u.)
RCD IgG
RCD α-DBI
MCD IgG
MCD α-DBI
F
RCD α-DBI vs. RCD IgG
MCD IgG vs. RCD IgG
MCD α-DBI vs. MCD IgG
Reduced by α-DBI
Enhanced by α-DBI
Reduced by MCD
Enhanced by MCD
- log10 (pvalue)
-log10 (p-value)
Log2 (Fold change)
Nlrp3
Cd68
Sod2
Mcp1
Hmox1
Tnfa
F480
Gsr
Sod1
Nfr2
Il6
Cat
Il1b
Gpx
Acta2
Col1a1
Anti-oxidant
Fibrosis
Inflammation
Macrophages

Figure S4

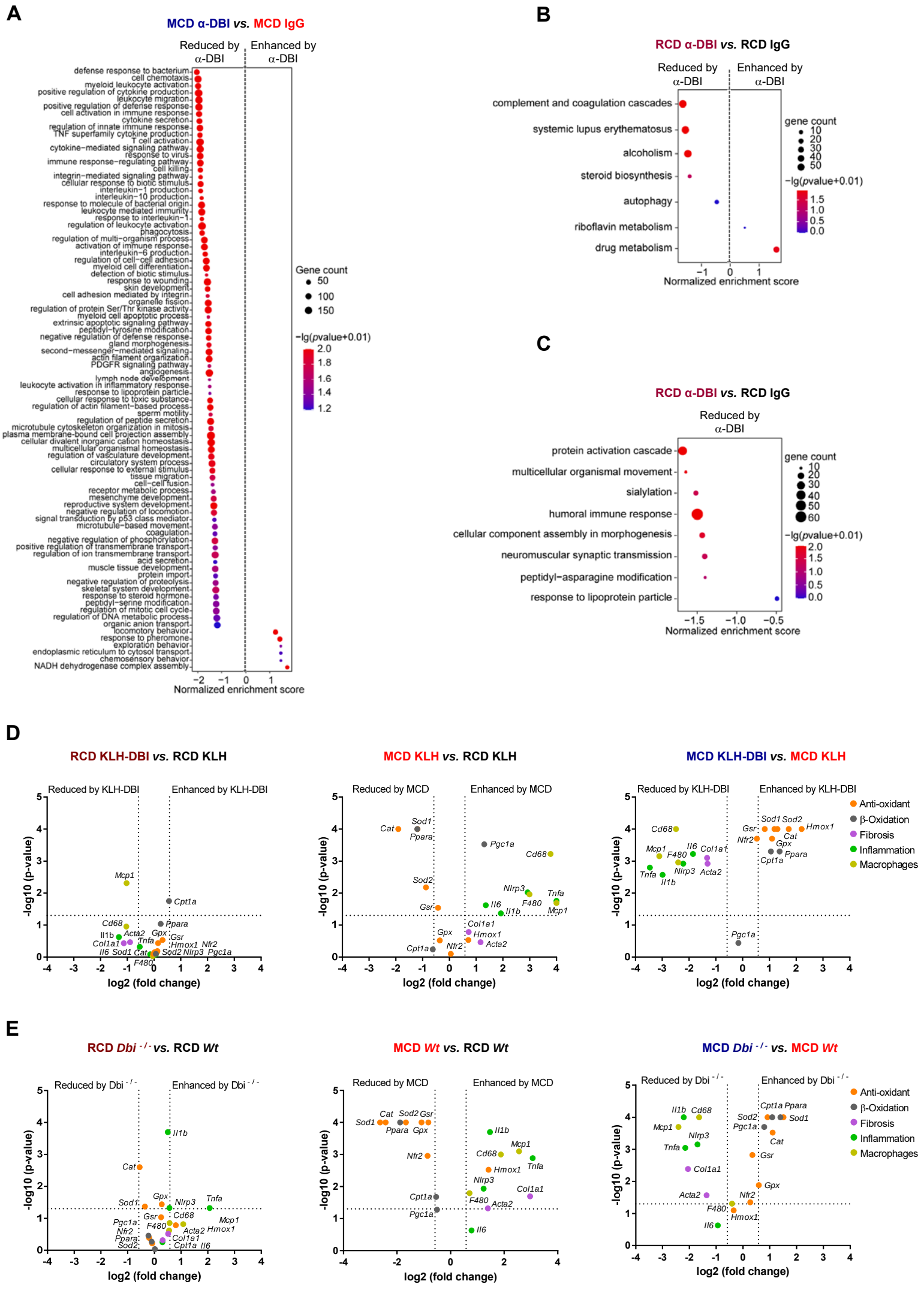
A
MCD α-DBI vs. MCD IgG
Reduced by α-DBI
Enhanced by α-DBI
defense response to bacterium
cell chemotaxis
myeloid leukocyte activation
positive regulation of cytokine production
leukocyte migration
positive regulation of defense response
cell activation in immune response
cytokine secretion
regulation of innate immune response
TNF superfamily cytokine production
T cell activation
cytokine−mediated signaling pathway
response to virus
immune response−regulating pathway
cell killing
integrin−mediated signaling pathway
cellular response to biotic stimulus
interleukin−1 production
interleukin−10 production
response to molecule of bacterial origin
leukocyte mediated immunity
response to interleukin−1
regulation of leukocyte activation
phagocytosis
regulation of multi−organism process
activation of immune response
interleukin−6 production
regulation of cell−cell adhesion
myeloid cell differentiation
detection of biotic stimulus
response to wounding
skin development
cell adhesion mediated by integrin
organelle fission
regulation of protein Ser/Thr kinase activity
myeloid cell apoptotic process
extrinsic apoptotic signaling pathway
peptidyl−tyrosine modification
negative regulation of defense response
gland morphogenesis
second−messenger−mediated signaling
actin filament organization
PDGFR signaling pathway
angiogenesis
lymph node development
leukocyte activation in inflammatory response
response to lipoprotein particle
cellular response to toxic substance
regulation of actin filament−based process
sperm motility
regulation of peptide secretion
microtubule cytoskeleton organization in mitosis
plasma membrane−bound cell projection assembly
cellular divalent inorganic cation homeostasis
multicellular organismal homeostasis
regulation of vasculature development
circulatory system process
cellular response to external stimulus
tissue migration
cell−cell fusion
receptor metabolic process
mesenchyme development
reproductive system development
negative regulation of locomotion
signal transduction by p53 class mediator
microtubule−based movement
coagulation
negative regulation of phosphorylation
positive regulation of transmembrane transport
regulation of ion transmembrane transport
acid secretion
muscle tissue development
protein import
negative regulation of proteolysis
skeletal system development
response to steroid hormone
peptidyl−serine modification
regulation of mitotic cell cycle
regulation of DNA metabolic process
organic anion transport
locomotory behavior
response to pheromone
exploration behavior
endoplasmic reticulum to cytosol transport
chemosensory behavior
NADH dehydrogenase complex assembly
−2 −1 0 1
Normalized enrichment score
Gene count
50
100
150
−lg(pvalue+0.01)
2.0
1.8
1.6
1.4
1.2
B
RCD α-DBI vs. RCD IgG
Reduced by α-DBI
Enhanced by α-DBI
complement and coagulation cascades
systemic lupus erythematosus
alcoholism
steroid biosynthesis
autophagy
riboflavin metabolism
drug metabolism
−1 0 1
Normalized enrichment score
gene count
10
20
30
40
50
−lg(pvalue+0.01)
1.5
1.0
0.5
0.0
C
RCD α-DBI vs. RCD IgG
Reduced by α-DBI
protein activation cascade
multicellular organismal movement
sialylation
humoral immune response
cellular component assembly in morphogenesis
neuromuscular synaptic transmission
peptidyl−asparagine modification
response to lipoprotein particle
−1.5 −1.0 −0.5
Normalized enrichment score
gene count
10
20
30
40
50
60
−lg(pvalue+0.01)
2.0
1.5
1.0
0.5
0.0
D
RCD KLH-DBI vs. RCD KLH
Reduced by KLH-DBI
Enhanced by KLH-DBI
-log10 (p-value)
log2 (fold change)
Mcp1
Cpt1a
Cd68
Ppara
Il1b
Acta2
Gpx
Gsr
Col1a1
Tnfa
Hmox1
Nfr2
Il6
Sod1
Cat
Sod2
Nlrp3
Pgc1a
F480
MCD KLH vs. RCD KLH
Reduced by MCD
Enhanced by MCD
-log10 (p-value)
log2 (fold change)
Cat
Sod1
Ppara
Pgc1a
Cd68
Sod2
Nlrp3
Tnfa
Gsr
Il6
F480
Il1b
Mcp1
Col1a1
Gpx
Hmox1
Cpt1a
Nfr2
Acta2
MCD KLH-DBI vs. MCD KLH
Reduced by KLH-DBI
Enhanced by KLH-DBI
-log10 (p-value)
log2 (fold change)
Cd68
Sod1
Sod2
Hmox1
Gsr
Cat
Nfr2
Gpx
Mcp1
Il6
Col1a1
F480
Ppara
Cpt1a
Tnfa
Nlrp3
Acta2
Il1b
Pgc1a
Anti-oxidant
β-Oxidation
Fibrosis
Inflammation
Macrophages
E
RCD Dbi -/- vs. RCD Wt
Reduced by Dbi -/-
Enhanced by Dbi -/-
-log10 (p-value)
log2 (fold change)
Il1b
Cat
Sod1
Gpx
Nlrp3
Tnfa
Pgc1a
Gsr
Cd68
Mcp1
Nfr2
F480
Acta2
Hmox1
Ppara
Col1a1
Sod2
Cpt1a
Il6
MCD Wt vs. RCD Wt
Reduced by MCD
Enhanced by MCD
-log10 (p-value)
log2 (fold change)
Cat
Sod2
Gsr
Sod1
Ppara
Gpx
Il1b
Mcp1
Nfr2
Cd68
Tnfa
Hmox1
Nlrp3
Col1a1
Cpt1a
F480
Acta2
Pgc1a
Il6
MCD Dbi -/- vs. MCD Wt
Reduced by Dbi -/-
Enhanced by Dbi -/-
-log10 (p-value)
log2 (fold change)
Il1b
Cd68
Cpt1a
Ppara
Sod2
Sod1
Mcp1
Pgc1a
Nlrp3
Cat
Tnfa
Gsr
Col1a1
Gpx
Acta2
Nfr2
F480
Hmox1
Il6
Anti-oxidant
β-Oxidation
Fibrosis
Inflammation
Macrophages

Figure S5

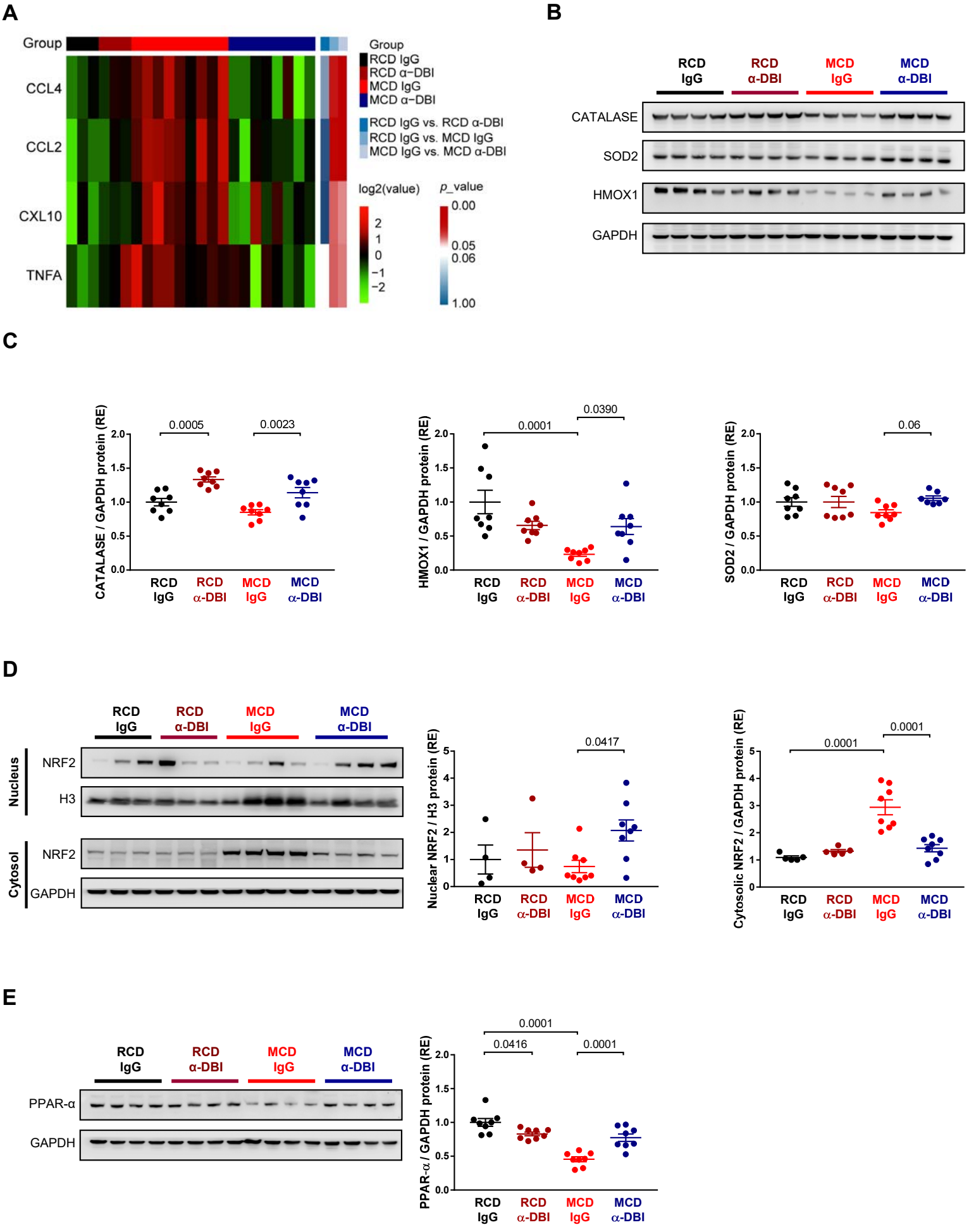
A
Group
CCL4
CCL2
CXL10
TNFA
Group
RCD IgG
RCD α−DBI
MCD IgG
MCD α−DBI
RCD IgG vs. RCD α-DBI
RCD IgG vs. MCD IgG
MCD IgG vs. MCD α-DBI
log2(value)
2
1
0
−1
−2
p_value
0.00
0.05
0.06
1.00
B
RCD IgG
RCD α-DBI
MCD IgG
MCD α-DBI
CATALASE
SOD2
HMOX1
GAPDH
C
CATALASE / GAPDH protein (RE)
0.0005
0.0023
HMOX1 / GAPDH protein (RE)
0.0001
0.0390
SOD2 / GAPDH protein (RE)
0.06
RCD IgG
RCD α-DBI
MCD IgG
MCD α-DBI
D
Nucleus
NRF2
H3
Cytosol
NRF2
GAPDH
Nuclear NRF2 / H3 protein (RE)
0.0417
Cytosolic NRF2 / GAPDH protein (RE)
0.0001
0.0001
E
PPAR-α
GAPDH
PPAR-α / GAPDH protein (RE)
0.0001
0.0416
0.0001

Figure S6

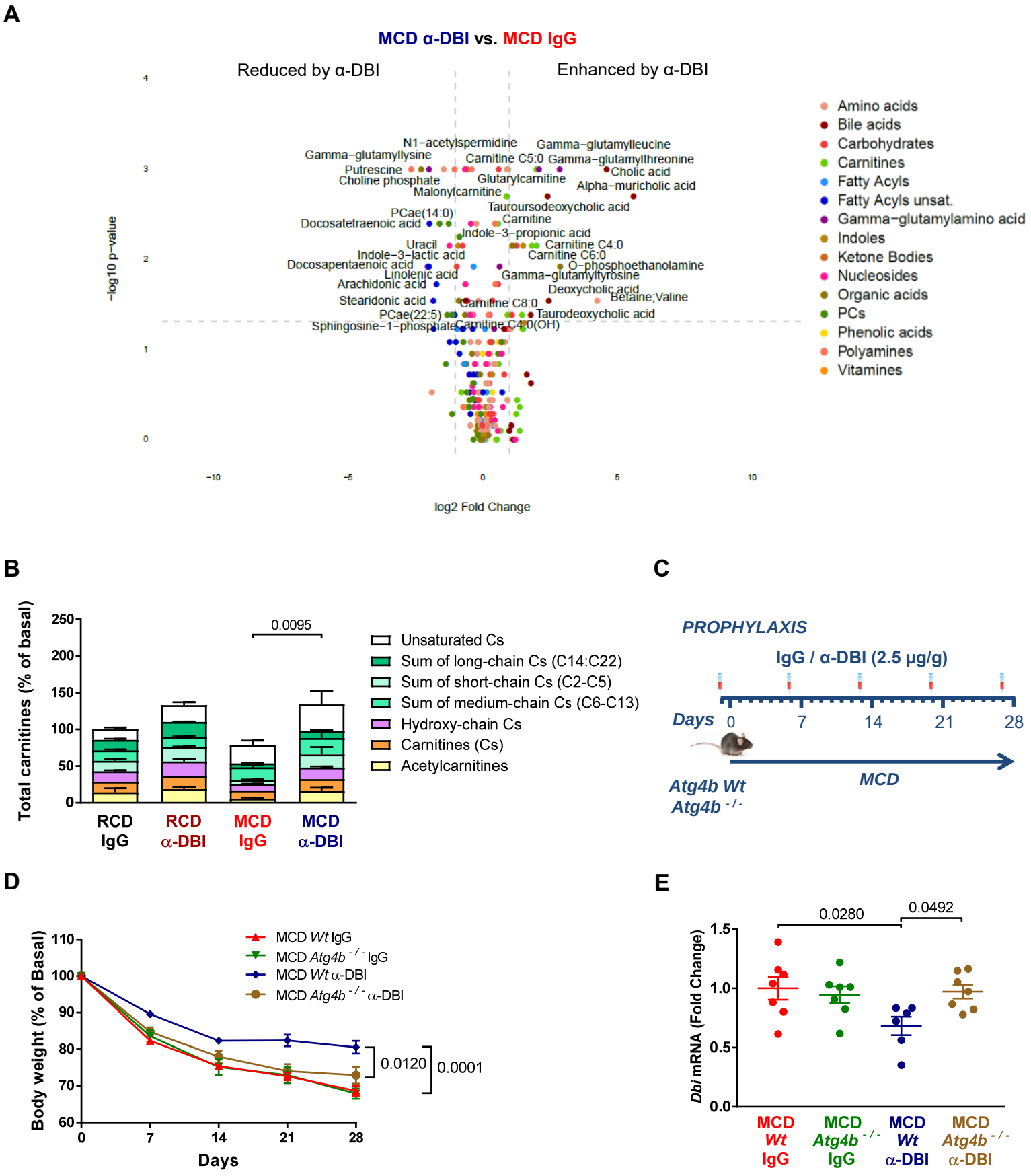
A
MCD α-DBI vs. MCD IgG
Reduced by α-DBI
Enhanced by α-DBI
−log10 p−value
log2 Fold Change
N1−acetylspermidine
Gamma−glutamylleucine
Gamma−glutamyllysine
Carnitine C5:0
Gamma−glutamylthreonine
Putrescine
Cholic acid
Choline phosphate
Glutarylcarnitine
Alpha−muricholic acid
Malonylcarnitine
Tauroursodeoxycholic acid
PCae(14:0)
Docosatetraenoic acid
Carnitine
Indole−3−propionic acid
Uracil
Carnitine C4:0
Indole−3−lactic acid
Carnitine C6:0
Docosapentaenoic acid
O−phosphoethanolamine
Linolenic acid
Gamma−glutamyltyrosine
Arachidonic acid
Deoxycholic acid
Stearidonic acid
Betaine;Valine
Carnitine C8:0
PCae(22:5)
Taurodeoxycholic acid
Sphingosine−1−phosphate
Carnitine C4:0(OH)
Amino acids
Bile acids
Carbohydrates
Carnitines
Fatty Acyls
Fatty Acyls unsat.
Gamma−glutamylamino acid
Indoles
Ketone Bodies
Nucleosides
Organic acids
PCs
Phenolic acids
Polyamines
Vitamines
B
Total carnitines (% of basal)
0.0095
RCD IgG
RCD α-DBI
MCD IgG
MCD α-DBI
Unsaturated Cs
Sum of long-chain Cs (C14:C22)
Sum of short-chain Cs (C2-C5)
Sum of medium-chain Cs (C6-C13)
Hydroxy-chain Cs
Carnitines (Cs)
Acetylcarnitines
C
PROPHYLAXIS
IgG / α-DBI (2.5 µg/g)
Days
0
7
14
21
28
MCD
Atg4b Wt
Atg4b -/-
D
Body weight (% of Basal)
MCD Wt IgG
MCD Atg4b -/- IgG
MCD Wt α-DBI
MCD Atg4b -/- α-DBI
0.0120
0.0001
Days
E
Dbi mRNA (Fold Change)
0.0280
0.0492
MCD Wt IgG
MCD Atg4b -/- IgG
MCD Wt α-DBI
MCD Atg4b -/- α-DBI

Figure S7

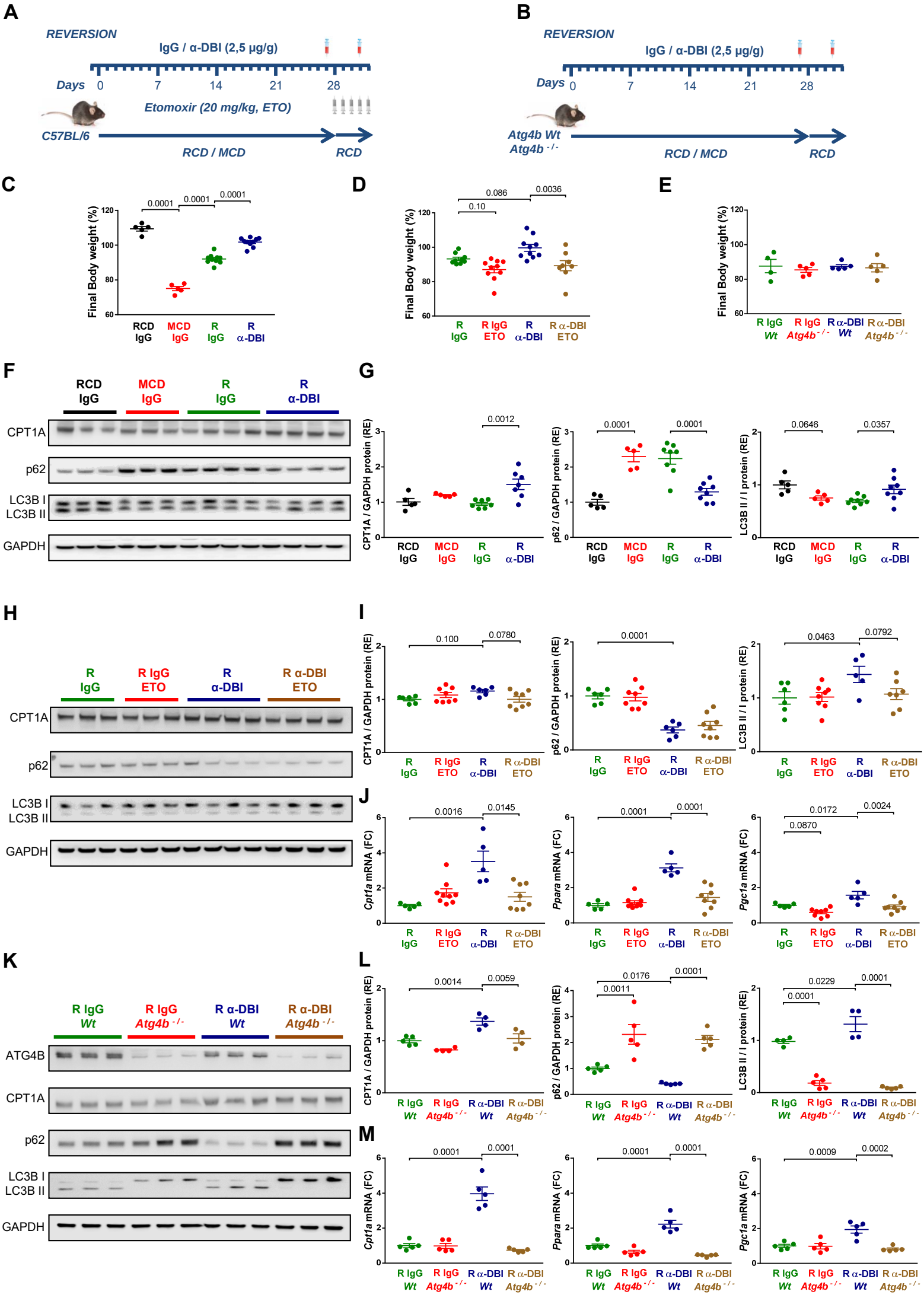
A
REVERSION
IgG / α-DBI (2,5 µg/g)
Days 0 7 14 21 28
Etomoxir (20 mg/kg, ETO)
C57BL/6
RCD / MCD
RCD
B
REVERSION
IgG / α-DBI (2,5 µg/g)
Days 0 7 14 21 28
Atg4b Wt
Atg4b -/-
RCD / MCD
RCD
C
Final Body weight (%)
0.0001
0.0001
0.0001
RCD IgG
MCD IgG
R IgG
R α-DBI
D
Final Body weight (%)
0.086
0.0036
0.10
R IgG
R IgG ETO
R α-DBI
R α-DBI ETO
E
Final Body weight (%)
R IgG Wt
R IgG Atg4b -/-
R α-DBI Wt
R α-DBI Atg4b -/-
F
RCD IgG
MCD IgG
R IgG
R α-DBI
CPT1A
p62
LC3B I
LC3B II
GAPDH
G
CPT1A / GAPDH protein (RE)
0.0012
p62 / GAPDH protein (RE)
0.0001
0.0001
LC3B II / I protein (RE)
0.0646
0.0357
H
R IgG
R IgG ETO
R α-DBI
R α-DBI ETO
CPT1A
p62
LC3B I
LC3B II
GAPDH
I
CPT1A / GAPDH protein (RE)
0.100
0.0780
p62 / GAPDH protein (RE)
0.0001
LC3B II / I protein (RE)
0.0463
0.0792
J
Cpt1a mRNA (FC)
0.0016
0.0145
Ppara mRNA (FC)
0.0001
0.0001
Pgc1a mRNA (FC)
0.0172
0.0024
0.0870
K
R IgG Wt
R IgG Atg4b -/-
R α-DBI Wt
R α-DBI Atg4b -/-
ATG4B
CPT1A
p62
LC3B I
LC3B II
GAPDH
L
CPT1A / GAPDH protein (RE)
0.0014
0.0059
p62 / GAPDH protein (RE)
0.0176
0.0001
0.0011
LC3B II / I protein (RE)
0.0229
0.0001
0.0001
M
Cpt1a mRNA (FC)
0.0001
0.0001
Ppara mRNA (FC)
0.0001
0.0001
Pgc1a mRNA (FC)
0.0009
0.0002

Figure S8

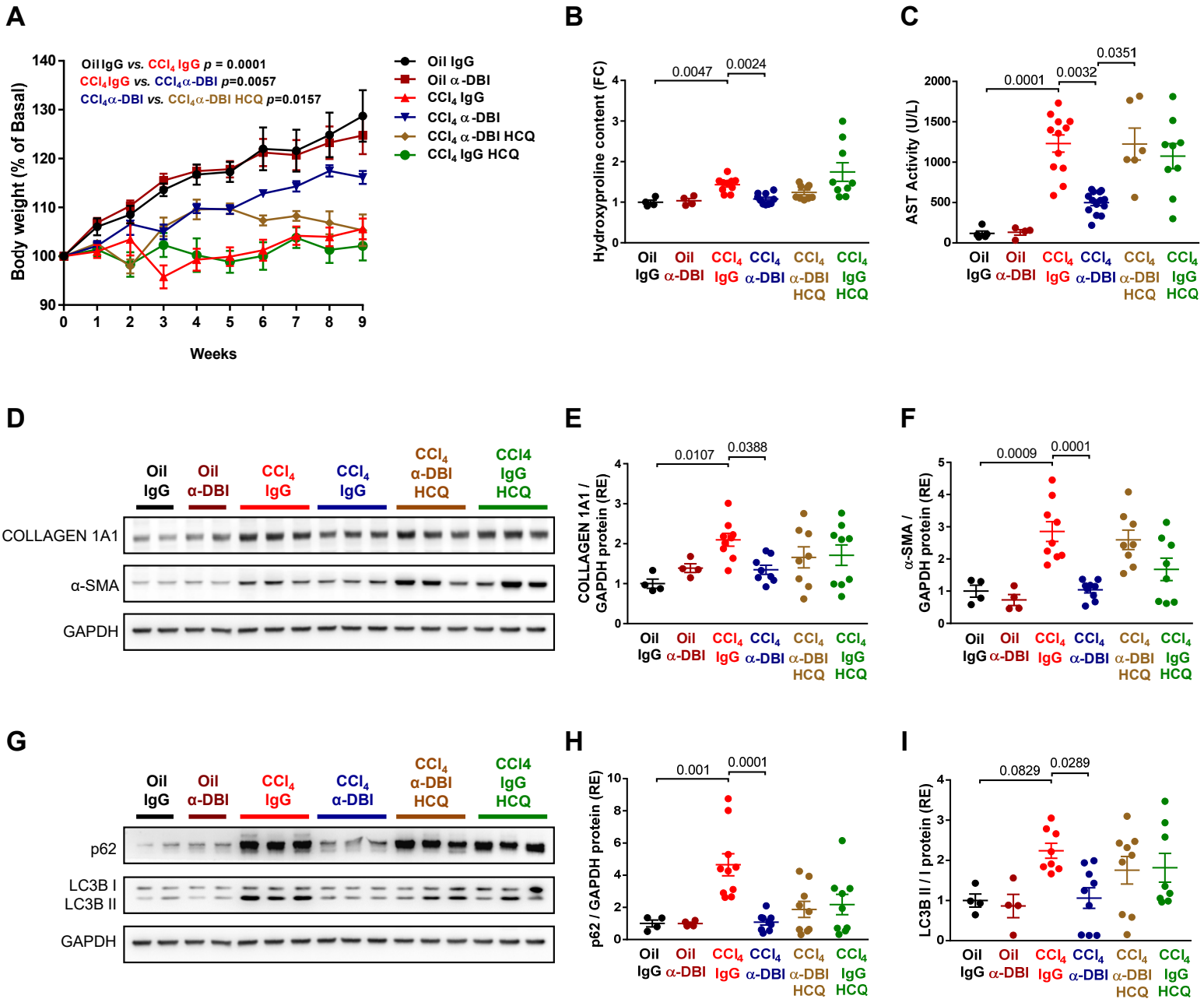
A
Oil IgG vs. CCl4 IgG p = 0.0001
CCl4 IgG vs. CCl4 α-DBI p=0.0057
CCl4 α-DBI vs. CCl4 α-DBI HCQ p=0.0157
Oil IgG
Oil α-DBI
CCl4 IgG
CCl4 α-DBI
CCl4 α-DBI HCQ
CCl4 IgG HCQ
Body weight (% of Basal)
Weeks
B
Hydroxyproline content (FC)
0.0047
0.0024
C
AST Activity (U/L)
0.0001
0.0032
0.0351
D
COLLAGEN 1A1
α-SMA
GAPDH
E
COLLAGEN 1A1 / GAPDH protein (RE)
0.0107
0.0388
F
α-SMA / GAPDH protein (RE)
0.0009
0.0001
G
p62
LC3B I
LC3B II
GAPDH
H
p62 / GAPDH protein (RE)
0.001
0.0001
I
LC3B II / I protein (RE)
0.0829
0.0289

Supplemental Figure Legends

Figure S1. α-DBI alleviates the hepatotoxicity induced by acetaminophen and concanavalin A *in vivo*.

A Experimental procedure of the damage induced by acetaminophen (APAP, i.p. 300 mg/kg for 16 hours) or concanavalin A (ConA, i.v.12 mg/kg for 4 hours) in mice pre-treated with i.p. injection of α-DBI or IgG (2.5 µg/g) and HCQ (50 mg/kg) for 4 hours and just before hepatic injury.

B-E Hepatoprotective effect of DBI neutralization after APAP intoxication. Representative images of HES staining **(B)** from mice pre-treated with α-DBI or IgG and HCQ and after APAP. The hepatic injury **(C)** was measured by histological examination taking account the area of cell death, degeneration (ballooning), and inflammation around the central veins. ALT and AST transaminases activity **(D** and **E)** from plasma mice (n=4-9 mice per group).

F-I Liver protection against ConA-damage by DBI neutralization. Histological pictures of HES staining **(F)** from mice pre-treated with α-DBI or IgG and HCQ and after ConA. Liver injury **(G)** was scored using grades of infiltration and hepatocyte necrosis. Activity of ALT and AST transaminases **(H** and **I)** in plasma (n=3-11 mice per group).

Necrotic areas are marked with asterisks, ballooning with arrowheads, and vascular congestion with arrows.

Data are expressed as means ± SEM. Statistical analyses (*p* values) were performed ANOVA **(C, G, I)** or Kruskal-Wallis test **(D-E, H)**.

Figure S2. ACBP/DBI inhibition reduces the loss weight caused by MCD and knockout of ACBP/DBI protects against NASH.

A-D Body weight **(A)** and hepatic mRNA levels of DBI **(B)** from mice treated with a-DBI or IgG as indicated in Fig. 2A (n=4-10 mice per group). Representation of the body weight **(C)** and mRNA levels of *Dbi* in the liver **(D)** from $Dbi^{-/-}$ and *Wt* mice (n=6-16 mice per group).

E-N DBI neutralization with antibodies improve NASH damaged derived by MCD. To induce the production of autoantibodies against DBI, the conjugation of recDBI and keyhole limpet hemocyanin (KLH-DBI) or KHL (control) was i.p. administrated weekly to C57BL/6 mice for 4 weeks. After autoimmunization, mice were fed with MCD for 4 weeks **(E)**. The body weight **(F)**, levels of hepatic *Dbi* mRNA **(G)**, representative western blots **(H)** and protein levels of p62 **(I)** and LC3 II/I **(J)** was measured in mice after KLH or KLH-DBI. Histological liver sections stained with HES **(K)**, NAFLD activity score **(L)** and plasma ALT **(M)** were analyzed (n=4-10 mice per group). *Wt* and $Gabrg2^{F77I/F77I}$ ($Gabrg2^{Mut/Mut}$) mice were fed with MCD for 4 weeks. HES histology images **(N)**, NAFLD score **(O)** and ALT activity **(P)** are shown after MCD (n=5-10 mice per group).

Asterisks, arrows, and arrowheads show inflammation foci, macro-steatosis, and micro-steatosis vesicular, respectively.

Results are displayed as means ± SEM. Statistical analyses (*p* value) were calculated by ANOVA test.

Figure S3. Whole transcriptome sequencing reflects a differential gene expression profile in mice treated with α-DBI after MCD.

A-B Heat map **(A)** of the two-way hierarchical clustering (1159 genes satisfying with fold change ≥ ± 1.5 and with $p < 0.05$) using Z scores for normalized values from mice fed with RCD or MCD and injected with IgG or α-DBI. Volcano plots comparing mRNA expression levels **(B)** between two groups in mice administrated with α-DBI *versus* IgG and fed with MCD (n=5 mice in each group).

C GSEA-based KEGG pathway enrichment analysis for RNA-seq data. RNA-seq was performed to analyze the differential expression of 54325 genes in liver samples obtained from Ig and α-DBI groups with MCD. The most significant pathways are shown.

D-E Representative hepatic images **(D)** and intensity quantification of F4/80 immunohistochemistry **(E)** from all mice on RCD or MCD treated with a-DBI (n=5-10 mice per group).

F Analysis of genes involved in inflammation (*Cd68, F480, Il1b, Il6, Mcp1, Nrlp3*, *Tnfa*), antioxidant responses (*Cat, Hmox1, Nrf2, Gpx, Gsr, Sod1, Sod2*) and fibrosis (*Col1a1, Acta2*) by RT-qPCR. Volcano plots are depicted with the fold change of each gene and the p value was calculated by performing a two-tailed unpaired Student's t test. The setting of threshold for $\log^2$ (fold change) is ±0.58 (cut-off value 1.5) and for −log10 (p value) was 1.3 (p value <0.05). The means of the mRNA expression data were compared between the indicated groups (n=3-6 mice per group). Results are represented as means ± SEM. Statistical analyses (*p* value) were calculated by Fisher's exact test **(B-C)**, ANOVA test **(E)** or two-tailed unpaired Student's t test **(F)**.

Figure S4. Analysis of gene expression profile in mice treated with α-DBI after MCD.

A-C GSEA-based KEGG/GO enrichment analysis for RNA-seq data. The differential expression of 54325 genes in liver samples, obtained from MCD plus IgG /α-DBI or RCD plus IgG/α-DBI groups, were determined by RNA-seq analysis. Then GSEA-based GO enrichment analysis on biological process (**A**: MCD α-DBI vs. MCD IgG; **C**: RCD α-DBI vs. RCD IgG) or KEGG pathway analysis (**B**: RCD α-DBI vs. RCD IgG) were performed to select the significant categories (*p* value < 0.05, Fisher's exact test).

D-E Volcano plots of genes related with inflammation (*Cd68, F480, Il1b, Il6, Mcp1, Nrlp3, Tnfa*), antioxidant response (*Cat, Hmox1, Nrf2, Gpx, Gsr, Sod1, Sod2*), fibrosis (*Col1a1 and Acta2*), and β-oxidation (*Cpt1a, Pgc1a, Ppara*) were measured by RT-qPCR. The means of the mRNA expression data were compared between the indicated groups (n=4-8 mice per group). *p* values were calculated by two-tailed unpaired Student's t test.

Figure S5. Analysis of pro-inflammatory cytokines and antioxidant enzymes in mice treated with α-DBI under MCD diet.

A Heatmap clustered by Euclidean distance of the plasmatic levels of CCL4, CCL2, CXCL10 and TNFA assessed by Luminex analysis (n=3-8 mice per group).

B-C Representative immunoblots **(B)** and densitometric analysis of CATALASE, HMOX1 and SOD2 **(C)** (n=7-8 mice per condition).

D Analysis of hepatic NRF2 translocation by Western blot from nuclear and cytosolic extracts (n=4-8 mice per condition).

E Representative Western Blot of PPARα from total liver extracts (n=8 mice per condition).

Data are expressed as means ± SEM. Statistical analyses (*p* values) were performed ANOVA.

Figure S6. Effects of α-DBI on liver metabolites.

A-B α-DBI increases the hepatic levels of carnitines. Volcano plot of metabolites **(A)** grouped by categories, comparing MCD-fed mice group treated with α-DBI (n=9) or IgG (n=5). The setting of thresholds for log^2 (Fold change) is ±0.58 (cut-off value 1.5) and for −Log10 (p value) was 1.3 (p value <0.05). Total carnitines and family carnitines are shown **(B)** (n=3-9 per condition).

C-E Schematic figure from *Atg4b*$^{-/-}$ and *Wt* mice treated every week with α-DBI and IgG plus MCD diet for 4 weeks **(C)**. Body weight **(D)** and hepatic mRNA levels of *Dbi* **(E)** from mice treated α-DBI and IgG with MCD diet (n=6-8 per group).

Data are displayed as means ± SEM. Statistical analyses (*p* values) were calculated by means of the two-tailed unpaired Mann Whitney test **(A)** or ANOVA test **(B, D-E)**.

Figure S7. α-DBI enhanced the recovery of NASH in an autophagy-dependent fashion.

A-B Experimental strategy of the NASH reversion (R) induced by MCD for 4 weeks plus 4 days with RCD. C57BL/6 **(A)** and *Atg4b*$^{-/-}$ **(B)** mice were injected i.p. with α-DBI or IgG (2.5 µg/g) one day before RCD and one day before sacrifice. Additionally, etomoxir (ETO) was administrated i.p every day for 4 days in mice fed with RCD.

C-E Final body weight represented as % of basal body weight from C57BL/6 **(C)** plus ETO **(D)** and *Atg4b*$^{-/-}$ **(E)** mice (n=4-10 mice per group).

F-G Representative immunoblots **(F)** and densitometric quantification **(G)** of CPT1A, p62 and LC3B from liver extracts in mice treated with α-DBI and IgG (n=5-8 mice per condition).

H-I Hepatic CPT1A, p62 and LC3B proteins levels analyzed by Western Blot from C57BL/6 mice treated with α-DBI and IgG plus ETO (n=5-8 mice per treatment).

J mRNA levels of genes involved in β-oxidation such as *Cpt1a*, *Ppara* and *Pgc1a* in the liver (n=5-9 mice per group).

K-M CPT1A, p62 and LC3B proteins levels (**K** and **L**) and *Cpt1a*, *Ppara* and *Pgc1a* mRNA expression **(M)** analyzed by Western Blot and RT-qPCR respectively from liver of *Atg4b*$^{-/-}$ mice treated with α-DBI and IgG (n=4-5 mice per group).
Data are displayed as means ± SEM. For statistical results, *p* values were calculated by ANOVA test **(C-D, G, I-J, L-M)** or Kruskal-Wallis test **(J)**.

Figure S8. ACBP/DBI neutralization prevents hepatic fibrosis in an autophagy-dependent fashion.
A-C Body weight **(A)**, levels of hydroxyproline **(B)**, and AST activity **(C)** after CCl_4 treatment in prophylaxis model (n=4-14 mice per condition).
D-F Representative Western blot (**D**) and densitometric analysis of COLLAGEN 1A1 **(E)** and α-SMA **(F)** from livers in prophylaxis condition (n=4-10 mice per group).
G-I Liver immunoblots **(G)** and densitometric analysis of p62 **(H)** and LC3B **(I)** from mice treated with α-DBI or IgG plus HCQ in prophylaxis (n=4-10 mice per group).
For statistical analyses, *p* values were calculated by ANOVA test **(A, E-F, H)** or Kruskal-Wallis test **(B-C, I).**

Table S1. ACBP/DBI neutralization downregulates genes that are upregulated in human NAFLD or NASH.

	GEO accession	No. of normal livers (NL)	No. of NASH livers	No. of NAFLD livers	No. of genes over-expressed in NASH/ NAFLD (P<0.05)	No. of genes reduced by anti-DBI in mouse MCD (p<0.05)	Overlap between data-sets	No. of genes analyzed in GEO datasets	No. of genes in mouse experi-ment	No. of unique genes in both groups	Overlap overrepre-sentation factor*	P value#
1	GSE159676	6	7	—	1484		230	17046		54710	2.13105	**6.28E-28**
2	GSE151158	21	—	40	239		106	618		54444	6.05636	**7.02E-56**
3	GSE63067	7	9	—	1587		345	54675		61524	3.35460	**4.74E-91**
4	GSE48452	14	18	—	1487		360	33297		59696	3.62485	**7.04E-106**
5	GSE17470	4	7	—	2618		484	44530		59677	2.76717	**8.12E-97**
6	GSE66676	34	7	26	899	3987	113	28869	54325	59000	1.86005	**1.78E-10**
7	GSE24807	5	12	—	3333		667	40346		59286	2.97575	**6.89E-153**
8	GSE33814	13	12	—	4380		1031	48803		58555	3.45702	**2.85E-306**
9	GSE126848	14	16	15	2581		598	19697		57744	3.35563	**1.53E-162**
10	GSE135251	10	—	206	4685		931	59913		76362	3.80602	**9.39E-300**
Sum					13350		2393	46943		84510	3.79947	**0**

* Overlap overrepresentation factor is ratio between actual overlap over theoretical overlap.

The p values were calculated with Fisher's exact test.

Table S2. List of reagents or resources used in the article.

REAGENT or RESOURCE	SOURCE	IDENTIFIER
Antibodies		
Anti-ACBP/DBI antibody	Abcam	ab231910
Anti-aSMA antibody	Sigma Aldrich	A2547
Anti-ATG4B antibody	Cell Signaling Technology	13507
Anti-CATALASE	Cell Signaling Technology	14097
Anti-COLLAGEN 1A1 antibody	Sigma Aldrich	234167
Anti-CPT1A antibody	Abcam	ab128568
Anti-F4/80 antibody	BioRad	MCA497G
Anti-GAPDH antibody	Cell Signaling Technology	2118
Anti-MAP1LC3B antibody	Cell Signaling Technology	2775
Anti-p62/SQSTM1 antibody	Abnova	H00008878-M01
Anti-PPARa	Abcam	ab61182
Anti-SOD2	Cell Signaling Technology	13141
Goat Anti-Mouse IgG (H+L) secondary antibody	Southern Biotech	1031-05
Goat Anti-Rat IgG (H+L) secondary antibody	Southern Biotech	3050-05
Goat Anti-Rabbit IgG (H+L) secondary antibody	Southern Biotech	4050-05
IgG2a antibody (in vivo isotype control)	Bioxcell	BE0085
Monoclonal anti-ACBP/DBI (in vivo neutralization)	Fred Hutch Antibody Technology	N/A
Chemicals, Peptides, and Recombinant Proteins		
Acetaminophen (APAP, Paracetamol)	Sigma Aldrich	A7085
Bleomycin (Bleo)	Sigma Aldrich	B5507
Concanavalin (ConA)	Sigma Aldrich	C5275
Etomoxir sodium	Sigma Aldrich	E1905
Hydroxychloroquine sulfate	Axon Medchem BV	2432
Imject mcKLH Subunits	Thermo Scientific	77649

Montanide ISA 51 VG	SEPPIC	36362/FL2R3
Recombinant mouse ACBP/DBI	Custom-made	N/A
SuperSignal West Pico chemiluminescent substrate	Thermo Scientific	34579
SYBR Green Master Mix	Applied Biosystems	4367659
Tamoxifen Free Base	Sigma Aldrich	T5648
Critical Commercial Assays		
Alanine transaminase (ALT) kit	Randox	AL1200
Aspartate transaminase (AST) kit	Randox	AS1202
Bilirubin kit	Sigma Aldrich	MAK126
Hydroxyproline kit	Sigma Aldrich	MAK008
Milliplex Mouse Cytokine/Chemokine	Merck Millipore	MCYTMAG-70K-PX32
RNeasy Plus Mini kit	Qiagen	74134
SuperScript™ VILO™ cDNA Synthesis Kit	Invitrogen	11754050
Deposited data		
GEO number RNAseq	GSE194346	
Experimental models: Organisms/ Strains		
Acbp/Dbi $^{fl/fl}$ mice in which loxP sites flank *Acbp* exon 2	Ozgene	N/A
Atg4b-/- ^{C57BL}/6 mice	Gift of Dr. Carlos Lopez-Otin, University of Oviedo, Spain	N/A
Atg7c $^{fl/fl}$ mice	Tong *et al*., 2019	N/A
B6.Cg-Tg(UBC-cre/ERT2)1Ejb/1J mice	Jackson Laboratory, Bar Harbor, ME, USA	N/A
C57BL/6JOlaHsd mice	Envigo	5704F
Gabrg2tm1Wul/J GABAA g2+$^{/+}$ mice	Charles River Laboratory, Lentilly, France	N/A
Gabrg2tm1Wul/J GABAA g2F77I$^{/F77I}$ mice	Charles River Laboratory, Lentilly, France	N/A
Mito-Keima Tg mice	Tong *et al*., 2019	N/A
GFP-LC3 Tg mice	Mizushima *et al.*, 2004	N/A
Oligonucleotides		
qPCR oligonucleotides		

Acbp/Dbi: FOR 5' GAATTTGACAAAGCCGCTGAG 3'	This study	N/A
Acbp/Dbi: REV 5' CCCACAGTAGCTTGTTTGAAGTG 3'	This study	N/A
Acta2: FOR 5' CCCAGACATCAGGGAGTAATGG 3'	This study	N/A
Acta2: REV 5' TCTATCGGATACTTCAGCGTCA 3'	This study	N/A
Cat: FOR 5' GAACGAGGAGGAGAGGAAAC 3'	This study	N/A
Cat: REV 5' TGAAATTCTTGACCGCTTTC 3'	This study	N/A
Cd68: FOR 5' TGTCTGATCTTGCTAGGACCG 3'	This study	N/A
Cd68: REV 5' GAGAGTAACGGCCTTTTTGTGA 3'	This study	N/A
Col1a1: FOR 5' AATGGCACGGCTGTGTGCGA 3'	This study	N/A
Col1a1: REV 5' AGCACTCGCCCTCCCGTCTT 3'	This study	N/A
Col1a2: FOR 5' AGCAGGTCCTTGGAAACCTT 3'	This study	N/A
Col1a2: REV 5' AAGGAGTTTCATCTGGCCCT 3'	This study	N/A
Col6a1: FOR 5' TCGGTCACCACGATCAAGTA 3'	This study	N/A
Col6a1: REV 5' TACTTCGGGAAAGGCACCTA 3'	This study	N/A
Col6a2: FOR 5' GCTCCTGATTGGGGGACTCT 3'	This study	N/A
Col6a2: REV 5' CCAACACGAAATACACGTTGAC 3'	This study	N/A
Col6a3: FOR 5' GCTGCGGAATCACTTTGTGC 3'	This study	N/A
Col6a3: REV 5' CACCTTGACACCTTTCTGGGT 3'	This study	N/A
Cpt1a: FOR 5' TCAATCGGACCCTAGACACC 3'	This study	N/A
Cpt1a: REV 5' CTTTCGACCCGAGAAGACCT 3'	This study	N/A
Desmin: FOR 5' GTTTCAGACTTGACTCAGGCAG 3'	This study	N/A
Desmin: REV 5' TCTCGCAGGTGTAGGACTGG 3'	This study	N/A
F4/80: FOR 5' CTTTGGCTATGGGCTTCCAGTC 3'	This study	N/A
F4/80: REV 5' GCAAGGACAGAGTTTATCGTG 3'	This study	N/A
Gpx: FOR 5' ATCGACATCGAACCTGACAT 3'	This study	N/A
Gpx: REV 5' GAGTGCAGCCAGTAATCACC 3'	This study	N/A
Gsr: FOR 5' ATTGGCTGTGATGAGATGCT 3'	This study	N/A
Gsr: REV 5' GGTAGGATGAATGGCAACTG 3'	This study	N/A

Hmox1: FOR 5' AGGCTAAGACCGCCTTCCT 3'	This study	N/A
Hmox1: REV 5' TGTGTTCCTCTGTCAGCATCA 3'	This study	N/A
Il1: FOR 5' AGAAGCTGTGGCAGCTACCTG 3'	This study	N/A
Il1: REV 5' GGAAAAGAAGGTGCTCATGTCC 3'	This study	N/A
Il6: FOR 5' GAGGATACCACTCCCAACAGACC 3'	This study	N/A
Il6: REV 5' AAGTGCATCATCGTTGTTCATACA 3'	This study	N/A
Mcp1: FOR 5' TTAAAAACCTGGATCGGAACCAA 3'	This study	N/A
Mcp1: REV 5' GCATTAGCTTCAGATTTACGGGT 3'	This study	N/A
Nlrp3: FOR 5' ATTACCCGCCCGAGAAAGG 3'	This study	N/A
Nlrp3: REV 5' TCGCAGCAAAGATCCACACAG 3'	This study	N/A
Nrf2: FOR 5' TAGATGACCATGAGTCGCTTGC 3'	This study	N/A
Nrf2: REV 5' GCCAAACTTGCTCCATGTCC 3'	This study	N/A
Pdgfa: FOR 5' TGGCTCGAAGTCAGATCCACA 3'	This study	N/A
Pdgfa: REV 5' TTCTCGGGCACATGGTTAATG 3'	This study	N/A
Pdgfb: FOR 5' TTCCAGGAGTGATACCAGCTT 3'	This study	N/A
Pdgfb: REV 5' AGGGGGCGTGATGACTAGG 3'	This study	N/A
Pdgfra: FOR 5' TCCATGCTAGACTCAGAAGTCA 3'	This study	N/A
Pdgfra: REV 5' TCCCGGTGGACACAATTTTTC 3'	This study	N/A
Pdgfrb: FOR 5' TTCCAGGAGTGATACCAGCTT 3'	This study	N/A
Pdgfrb: REV 5' AGGGGGCGTGATGACTAGG 3'	This study	N/A
Pgc1a: FOR 5' AAGTGTGGAACTCTCTGGAACTG 3'	This study	N/A
Pgc1a: REV 5' GGGTTATCTTGGTTGGCTTTATG 3'	This study	N/A
Ppara: FOR 5' AGAGCCCCATCTGTCCTCTC 3'	This study	N/A
Ppara: REV 5' ACTGGTAGTCTGCAAAACCAAA 3'	This study	N/A
Sod1: FOR 5' TGTGTCCATTGAAGATCGTG 3'	This study	N/A
Sod1: REV 5' CTTTGCCCAAGTCATCTTGT 3'	This study	N/A
Sod2: FOR 5' TCAGTGCTCACTCGTGTCAT 3'	This study	N/A
Sod2: REV 5' ACACGATAGGTTTGGGCATA 3'	This study	N/A

Tnfa: FOR 5' CATCTTCTCAAAATTCGAGTGACAA 3'	This study	N/A
Tnfa: REV 5' TGGGAGTAGACAAGGTACAACCC 3'	This study	N/A
Vimentin: FOR 5' CGTCCACACGCACCTACAG 3'	This study	N/A
Vimentin: REV 5' GGGGGATGAGGAATAGAGGCT 3'	This study	N/A
Rplo/36b4: FOR 5' ACTGGTCTAGGACCCGAGAAG 3'	This study	N/A
Rplo/36b4: REV 5' TCCCACCTTGTCTCCAGTCT 3'	This study	N/A
Genotyping		
Cre: FOR 5' AGGTTCGTTCACTCATGGA 3'	This study	N/A
Cre: REV 5' TCGACCAGTTTAGTTACCC 3'	This study	N/A
GABRG2 knock-in: FOR 5' AAGCGCCCACCTCTACTTCT 3'	This study	N/A
GABRG2 knock-in: REV 5' TCATGGGATAGTGCATCAGC 3'	This study	N/A
Software and algorithms		
DESeq2 package	Love et al., 2014	N/A
Gene Ontology analysis (http://www.bioinformatics.com.cn)	Wang et al., 2017	N/A
HISAT2 algorithm (reference genome GRCm39)	Kim et al., 2019	N/A
Image J	National Institutes of Health	N/A
Metabolomic dataset analysis R (v3.4) package (@Github/Kroemerlab/GRMeta		
GraphPad Prism 7 software	Graph Pad Software Inc	N/A
QuPath 0.2.3 software	Centre for Cancer Research & Cell Biology at Queen's University Belfast	N/A
StepOne Software v2.3	Applied Biosystems	N/A
Zen 3.2 software	ZEISS	N/A
Others		
Precellys tissue homogenizing ceramic beads	Bertin Technologies	CKMix
Lithium heparin blood collection tubes	Sarstedt	6443
Luminex™ FLEXMAP 3D™ Instrument System	Merck Millipore	APX1342
Methione and choline deficiente diet (MCD)	Safe	AIN-76

Regular-chow Diet (RCD)	Safe	A04
StepOnePlus Real-Time PCR System	Applied Biosystems	N/A